

The granular column collapse as a continuum: validity of a two-dimensional Navier–Stokes model with a $\mu(I)$ -rheology

P.-Y. Lagrée^{1†}, L. Staron¹ and S. Popinet^{1,2}

¹ CNRS and UPMC Université Paris 06, UMR 7190, Institut Jean Le Rond d’Alembert,
Boîte 162, F-75005 Paris, France

² National Institute of Water and Atmospheric Research, PO Box 14-901 Kilbirnie,
Wellington, New Zealand

(Received 18 February 2011; revised 24 May 2011; accepted 3 August 2011;
first published online 27 September 2011)

There is a large amount of experimental and numerical work dealing with dry granular flows (such as sand, glass beads, etc.) that supports the so-called $\mu(I)$ -rheology. The reliability of the $\mu(I)$ -rheology in the case of complex transient flows is not fully ascertained, however. From this perspective, the granular column collapse experiment provides an interesting benchmark. In this paper we implement the $\mu(I)$ -rheology in a Navier–Stokes solver (Gerris) and compare the resulting solutions with both analytical solutions and two-dimensional contact dynamics discrete simulations. In a first series of simulations, we check the numerical model in the case of a steady infinite two-dimensional granular layer avalanching on an inclined plane. A second layer of Newtonian fluid is then added over the granular layer in order to recover a close approximation of a free-surface condition. Comparisons with analytical and semi-analytical solutions provide conclusive validation of the numerical implementation of the $\mu(I)$ -rheology. In a second part, we simulate the unsteady two-dimensional collapse of granular columns over a wide range of aspect ratios. Systematic comparisons with discrete two-dimensional contact dynamics simulations show good agreement between the two methods for the inner deformations and the time evolution of the shape during most of the flow, while a systematic underestimation of the final run-out is observed. The experimental scalings of spreading of the column as a function of the aspect ratio available from the literature are also recovered. A discussion follows on the performances of other rheologies, and on the sensitivity of the simulations to the parameters of the $\mu(I)$ -rheology.

Key words: granular media, Navier–Stokes equations, non-Newtonian flows

1. Introduction

Despite a large amount of dedicated research, modelling and predicting granular flows remains a challenging goal. Granular flows are characterized by a very large diversity of behaviours. For example, the simple controlled experiment of a granular layer flowing on an inclined plane reveals more intriguing features than one would

† Email address for correspondence: pierre-yves.lagree@upmc.fr

expect. As a consequence, defining a generic continuum granular flow rheology has not yet been achieved. Recurrent struggles are, for instance, the identification of a relevant variable to describe the transition from arrest to flow and the corresponding hysteresis, the initiation of shear banding, or the understanding of non-local effects (Aranson & Tsimring 2001; GdR MiDi 2004; Pouliquen & Forterre 2009).

Notwithstanding these difficulties, much progress has been made since the pioneering work of Bagnold (1954); however, these advances have primarily concerned phenomenological observations rather than reliable modelling. This includes the following topics: role of initial conditions and hysteretic behaviour, dependence on system size, wall effects, fluidization, etc. (Daerr & Douady 1999; Courrech du Pont *et al.* 2003; Jop, Forterre & Pouliquen 2005; Nichol *et al.* 2010). Constitutive laws that could explain and predict these observations are still lacking. Among the different models and theories developed in the past two decades, the $\mu(I)$ -rheology has recently emerged as the only framework so far consistently describing observations from a great variety of experimental and numerical set-ups (GdR MiDi 2004; Jop, Forterre & Pouliquen 2006; Pouliquen & Forterre 2009). Initially established for stationary shear flows, and based on a Coulombic friction model, this rheology relates the value of the effective coefficient of Coulombic friction μ (the ratio of tangential to normal stresses) to the non-dimensional inertial number I (comparing the typical time scale of microscopic rearrangements and the typical time scale of macroscopic deformations). Although the $\mu(I)$ -rheology is mostly phenomenological, it rests on a physical basis based on the origin of frictional properties. Most interestingly, its validity seems to extend to the case of highly dynamical and transient situations such as the granular column collapse, as shown by the numerical work of Lacaze & Kerswell (2009). The granular column collapse experiment was initially designed to constrain the factors controlling the run-out (or maximum distance reached by the flowing material) of natural catastrophic granular flows (Lajeunesse, Mangeney-Castelneau & Vilotte 2004; Lube *et al.* 2004). It simply consists of initially confined columns of grains allowed to spread over a horizontal plane in response to gravity. The main outcome can be summarized as follows. The run-out (normalized by the initial width of the column) behaves like a power law of the column initial aspect ratio (initial height to initial width); the exponent of the power law is dependent only on the geometry of the column; and its value is highly reproducible. Although the experimental set-up is simple, the origin of the power-law scaling is not fully understood. In the context of the present work, however, it offers a reference behaviour against which the $\mu(I)$ -rheology can be compared, provided we have a simulation tool solving this specific constitutive model. Continuum modelling of the granular column collapse has been the subject of several studies, often based on the Saint-Venant/shallow-layer approximation, whose validity is intrinsically limited to squat columns (Kerswell 2005; Mangeney-Castelneau *et al.* 2005; Larrieu, Staron & Hinch 2006; Doyle *et al.* 2007; Hogg 2007). Recently, two-dimensional simulations of the collapse of elastoplastic materials allowed for the modelling of tall columns with good agreement (Crosta, Imposimato & Roddeman 2009), but using a Lagrangian approach and a Mohr–Coulomb plastic model. Yet, no systematic comparisons between discrete granular dynamics and the complete Navier–Stokes equations with continuum rheologies were carried out. The challenge is no less than the simulation of granular systems (from silos to geophysical flows) at an affordable computational cost.

In this paper, we simulate numerically the two-dimensional granular column collapse experiment using the Gerris two-phase flow Navier–Stokes solver, in which we have implemented the non-Newtonian $\mu(I)$ -rheology. We consider the flow of dry granular

material, in contrast to Chauchat & Médale (2010), in which immersed granular flows were considered. The first validation results of this rheology are presented in § 2. We validate our approach by testing it against two ideal avalanche configurations: the case of a single granular layer on an incline, and the case of two layers (a granular layer covered by a viscous flow). Showing that the upper layer plays a negligible role for the range of parameters in which we are interested, we apply our approach to the more complex case of the transient flow of the granular column collapse in § 3. In parallel, we perform simulations using the discrete contact dynamics method (Moreau 1994), in which the motion of individual grains is explicitly solved, thus allowing detailed comparison with the continuum $\mu(I)$ counterpart (Staron & Hinch 2005, 2007). Details of the discrete numerical methods are presented as well. We compare experimental scaling laws for the run-out and the deposit height with the outcome of the continuum simulation. Comparisons with discrete simulations of the time evolution of the shape of the column are also performed. Other plausible candidate rheologies (Bagnold, Bingham, constant friction, and a case with linearized total derivative in the Navier–Stokes equations) are tested and their performances discussed. Finally, at the end of § 3 we present a detailed discussion on the sensitivity of the $\mu(I)$ -rheology to parameters, and on the difficulty of modelling the flow front from both a theoretical and a numerical point of view.

2. Implementing the $\mu(I)$ -rheology in a Navier–Stokes solver

2.1. Some results on the $\mu(I)$ -rheology

Early concepts to explain the behaviour of granular flows were introduced in the seminal work of Bagnold (1954), who identified many of the features of granular media by analysing field and laboratory experiments. Since this pioneering work, one of the major milestones might be the introduction of the so-called $\mu(I)$ -rheology by the Midi group (GdR MiDi 2004). Some of the ideas developed in that paper were to some extent already discussed in Savage (1979), Savage & Hutter (1989) and Ancy, Coussot & Evesque (1999); however, the $\mu(I)$ -rheology results from the analysis of a large number of experimental and numerical data sets, which for the first time revealed a common framework explaining a wide range of behaviours of granular materials. The prospect of these efforts is a comprehensive and reliable description of granular dynamics using a continuum mechanics point of view.

Granular media can flow as complex non-Newtonian fluids or resist shearing as a plastic solid. First, they are characterized by the existence of a flow threshold analogous to the classical Mohr–Coulomb friction law. When the flow develops, by analogy with Coulombic friction, the local normal stress p and the local tangential stress τ are often found in practice and assumed in the model to be proportional:

$$\tau = \mu p, \quad (2.1)$$

where μ is the analogue of a coefficient of friction. The introduction of a Coulomb-like friction law in a continuum description of granular flows is not new. It was first proposed by Savage & Hutter (1989), who derived shallow-layer equations for granular flows where dissipation was accounted for through basal friction. The value and physical origin of this basal coefficient of friction have subsequently been the subject of extensive work (Pouliquen & Forterre 2002; Bouchut *et al.* 2008; Kelfoun *et al.* 2009; Davies, McSaveney & Kelfoun 2010; Mangeney *et al.* 2010). The underlying question is which mechanisms at the grain scale in the bulk are responsible for dissipation and/or effective friction.

The strength and novelty of the $\mu(I)$ -rheology lay in the fact that it relates the effective coefficient of friction characterizing the flow to a non-dimensional number reflecting the local state of the granular packing. This number is known as the *inertial number* I (da Cruz 2004), and is defined as

$$I = \frac{d \partial u / \partial y}{\sqrt{p / \rho}}, \quad (2.2)$$

where $\partial u / \partial y$ is the shear rate, p is the pressure, and d and ρ are the diameter and the density of the grains, respectively. It represents the ratio of two time scales: $(\partial u / \partial y)^{-1}$ is a macroscopic shear deformation time scale, and $\sqrt{\rho d^2 / p}$ is an inertial time scale constructed with the pressure force $p d^2$. Gathering and comparing a large variety of studies of shear flows (Couette plane shear, annular shear, vertical chute flows, inclined plane, heap flow, rotating drum), either experimentally or numerically (using discrete methods such as molecular dynamics or contact dynamics simulations), GdR MiDi (2004) has demonstrated the generality of the dependence of the ratio τ / p on I . The following law was proposed as a possible fit to account for the shape of the dependence (Jop *et al.* 2005, 2006):

$$\mu(I) = \mu_s + \frac{\Delta\mu}{I_0 I + 1}, \quad (2.3)$$

where the values of the coefficients μ_s , $\Delta\mu$ and I_0 are material-dependent; indicative values for glass beads are $\mu_s = 0.38$, $\Delta\mu = 0.26$ and $I_0 = 0.279$ (Jop *et al.* 2005). Recently, numerical studies using discrete element simulations have shown that the $\mu(I)$ dependence was also satisfied in highly transient situations such as the granular column collapse (Lacaze & Kerswell 2009).

So far, the $\mu(I)$ -rheology is purely phenomenological. Other models exist, building on different theoretical backgrounds (Mills, Loggia & Tixier 1999; Aranson & Tsimring 2001; Josserand, Lagr e & Lhuillier 2006); however, none compares so well against so many experiments. Although the validity of the $\mu(I)$ -rheology might be questionable close to the jamming transition (Staron *et al.* 2010), or when non-local effects are not negligible (Pouliquen & Forterre 2009; Nichol *et al.* 2010), it emerges nonetheless as the most reliable description of granular flows so far. Therefore, in what follows, we will not discuss the validity of the $\mu(I)$ model. Instead, we will be interested in the still challenging issue of implementing a granular rheology in a continuum mechanics model, while going beyond the averaged Saint-Venant/shallow-layer approaches, which presents the shortcomings of a simplified description of the flow, and the need for a closure hypothesis. Following the idea of Jop *et al.* (2006), who generalize relations (2.2) in a tensorial way to obtain a constitutive law for granular flows, we implement the $\mu(I)$ -rheology in an incompressible two-dimensional Navier–Stokes solver and discuss the solution. Previous attempts to implement the $\mu(I)$ -rheology in Navier–Stokes solvers were hampered by the difficult coupling between a free-surface condition and the (pressure-dependent) $\mu(I)$ -rheology (O. Pouliquen 2009, personal communication; Cawthorn 2011). By reusing the two-fluid model implemented in the Gerris solver (Popinet 2009), we are able to circumvent this particular problem.

2.2. Implementing the viscosity in the Gerris flow solver

2.2.1. The Gerris flow solver

Gerris is an open-source solver for the solution of incompressible fluid motion using the finite-volume approach (Popinet 2003, 2009). Gerris uses the volume-of-fluid

(VOF) method to describe variable-density two-phase flows. In this method, the Navier–Stokes equations are written as

$$\nabla \cdot \mathbf{u} = 0, \quad (2.4)$$

$$\rho \left(\frac{\partial \mathbf{u}}{\partial t} + \mathbf{u} \cdot \nabla \mathbf{u} \right) = -\nabla p + \nabla \cdot (2\eta \mathbf{D}) + \rho \mathbf{g}, \quad (2.5)$$

$$\frac{\partial c}{\partial t} + \nabla \cdot (c\mathbf{u}) = 0, \quad (2.6)$$

$$\rho = c\rho_1 + (1 - c)\rho_2, \quad (2.7)$$

$$\eta = 1/[c/\eta_1 + (1 - c)/\eta_2], \quad (2.8)$$

where the volume fraction $c(x, y, t)$ enables the tracking of the position of the interface; the mixture viscosity is taken as the harmonic mean of the viscosities of each phase; and \mathbf{D} is the strain rate tensor, $(\nabla \mathbf{u} + \nabla \mathbf{u}^T)/2$.

The boundary condition will be supposed to be no-slip at the rigid walls (even if it is possible to implement a mixed Robin–Navier boundary condition). The pressure will be imposed at the top of the domain. In the case of avalanches, periodic conditions will be imposed. Other details will be given later, as they depend on the configuration.

2.2.2. Some details on the solver

Gerris uses a second-order staggered-in-time discretization combined with a time-splitting projection method. This gives the following time stepping scheme:

$$\frac{c_{n+\frac{1}{2}} - c_{n-\frac{1}{2}}}{\Delta t} + \nabla \cdot (c_n \mathbf{u}_n) = 0, \quad (2.9)$$

$$\rho_{n+\frac{1}{2}} \left(\frac{\mathbf{u}_* - \mathbf{u}_n}{\Delta t} + \mathbf{u}_{n+\frac{1}{2}} \cdot \nabla \mathbf{u}_{n+\frac{1}{2}} \right) = \nabla \cdot (\eta_{n+\frac{1}{2}} \mathbf{D}_*) - \nabla p_{n-\frac{1}{2}}, \quad (2.10)$$

$$\mathbf{u}_{n+1} = \mathbf{u}_* - \frac{\Delta t}{\rho_{n+\frac{1}{2}}} (\nabla p_{n+\frac{1}{2}} - \nabla p_{n-\frac{1}{2}}), \quad (2.11)$$

$$\nabla \cdot \mathbf{u}_{n+1} = 0. \quad (2.12)$$

Combining (2.11) and (2.12) of the above set results in the following Poisson equation:

$$\nabla \cdot \left(\frac{\Delta t}{\rho_{n+\frac{1}{2}}} \nabla p_{n+\frac{1}{2}} \right) = \nabla \cdot \left(\mathbf{u}_* + \frac{\Delta t}{\rho_{n+\frac{1}{2}}} \nabla p_{n-\frac{1}{2}} \right). \quad (2.13)$$

The momentum equation (2.10) can be reorganized as

$$\frac{\rho_{n+\frac{1}{2}}}{\Delta t} \mathbf{u}_* - \nabla \cdot (\eta_{n+\frac{1}{2}} \mathbf{D}_*) = \rho_{n+\frac{1}{2}} \left[\frac{\mathbf{u}_n}{\Delta t} - \mathbf{u}_{n+\frac{1}{2}} \cdot \nabla \mathbf{u}_{n+\frac{1}{2}} \right] - \nabla p_{n-\frac{1}{2}}, \quad (2.14)$$

where the velocity advection term $\mathbf{u}_{n+(1/2)} \cdot \nabla \mathbf{u}_{n+(1/2)}$ is estimated by means of the Bell–Colella–Glaz second-order unsplit upwind scheme (Bell *et al.* 1989; Popinet 2003). Note that the diffusion equation for \mathbf{u}_* , equation (2.14), uses a backward Euler implicit scheme that is stable for arbitrary values of η . This will be important when dealing with stiff rheologies such as $\mu(I)$. For Newtonian fluids, $\eta_{n+(1/2)}$ is a function of $c_{n+(1/2)}$. In the case of the $\mu(I)$ -rheology, it is computed using $c_{n+(1/2)}$, \mathbf{D}_n and p_n (so that the scheme is not strictly second-order in time any more).

Equation (2.13) is a Poisson-like problem with p as unknown variable, while (2.14) is similar to a Helmholtz problem with \mathbf{u}_* as unknown variable. An efficient multilevel

Poisson solver for (2.13) is described in Popinet (2003). However, it is only applicable to scalar fields and cannot be used directly to solve (2.14) to obtain the vector field \mathbf{u}_* . A work-around is to decouple the equations for each of the components of \mathbf{u}_* and then use the scalar multilevel algorithm to solve for each component independently. The equations for each component are coupled through the cross-terms $\nabla \mathbf{u}_*^T$ appearing in $\nabla \cdot (\eta_{n+(1/2)} \mathbf{D}_*)$ in (2.14). To obtain scalar Helmholtz-like problems for each component, we discretize the cross-terms explicitly such that the Laplacian operator in (2.14) is approximated as

$$2\nabla \cdot (\eta_{n+\frac{1}{2}} \mathbf{D}_*) \simeq \nabla \cdot (\eta_{n+\frac{1}{2}} \nabla \mathbf{u}_*) + \nabla \cdot (\eta_{n+\frac{1}{2}} \nabla \mathbf{u}_n^T). \quad (2.15)$$

The explicit cross-terms can be further rearranged, as we have the tensorial general identity

$$\nabla \cdot (\eta \nabla \mathbf{u}^T) = \nabla \mathbf{u}^T \nabla \eta + \eta \nabla \cdot \nabla \mathbf{u}^T = \nabla \mathbf{u}^T \nabla \eta + \eta \nabla (\nabla \cdot \mathbf{u}) = \nabla \mathbf{u}^T \nabla \eta, \quad (2.16)$$

where we have used the incompressibility condition $\nabla \cdot \mathbf{u} = 0$. The final decoupled scalar equations for each velocity component can then be written in vector form:

$$\begin{aligned} \frac{\rho_{n+\frac{1}{2}}}{\Delta t} \mathbf{u}_* - \frac{1}{2} \nabla \cdot (\eta_{n+\frac{1}{2}} \nabla \mathbf{u}_*) \\ = \rho_{n+\frac{1}{2}} \left[\frac{\mathbf{u}_n}{\Delta t} - \mathbf{u}_{n+\frac{1}{2}} \cdot \nabla \mathbf{u}_{n+\frac{1}{2}} \right] - \nabla p_{n-\frac{1}{2}} + \frac{1}{2} \nabla \mathbf{u}_n^T \nabla \eta_{n+\frac{1}{2}}. \end{aligned} \quad (2.17)$$

Note that the explicit viscous term on the right-hand side vanishes for a constant viscosity. For variable viscosities, it is only dependent on the viscosity gradient. The robustness of the implicit scheme is preserved for large values of viscosities provided the spatial viscosity variations are small enough. This scheme has been validated for numerous problems with variable viscosity such as two-phase flows of Newtonian fluids with different properties (Fuster *et al.* 2009a,b; Popinet 2009; Bagué *et al.* 2010), as well as generalized Newtonian fluids (Popinet 2005) including yield-stress rheologies (Josserand *et al.* 2009).

Space is discretized using an octree where the variables are located at the centre of each cubic discretization volume and are interpreted as the average value of the variable in the cell. Coupled with the VOF representation of interfaces, this finite-volume formulation guarantees mass and free stream conservation. The octree discretization used in Gerris allows an efficient mesh refinement or coarsening. The mesh can be adapted at every time step on demand with a minimal impact on overall performance. We refer the reader to Popinet (2003, 2009), and references therein, for a comprehensive presentation of the quad/octree data structure and the numerical integration procedure of the incompressible Navier–Stokes scheme.

2.2.3. The $\mu(I)$ -viscosity

The $\mu(I)$ -viscosity is constructed from the second invariant $D_2 = \sqrt{D_{ij} D_{ij}}$ of the strain rate tensor \mathbf{D} ($D_{ij} = (u_{i,j} + u_{j,i})/2$). Then, following Jop *et al.* (2005), we implement the expression of $\mu(I)$ and I into the Gerris solver, redefining the inertial number I using the second invariant D_2 as

$$\eta = \max \left(\frac{\mu(I)}{\sqrt{2} D_2} p, 0 \right) \quad \text{with } I = \frac{d\sqrt{2} D_2}{\sqrt{|p|/\rho}}. \quad (2.18)$$

In practice, the viscosity at very low shear rates is also bounded arbitrarily by $\eta_M = 250\rho\sqrt{gH^3}$, as real ‘solid-like’ behaviour cannot be described by viscosity

alone. Real arrest of the flow is thus approximated by a very slow creeping motion. All the results presented were checked to be insensitive to the exact value of η_M (down to values less than $\eta_M = 1.0\rho\sqrt{gH^3}$, which effectively produce noticeable creeping). Other regularizations may be constructed. Several non-Newtonian viscosities are implemented in the following simulations (Newtonian, Bagnold, Bingham, etc.).

2.2.4. Why use a two-phase model?

The imposition of accurate free-surface boundary conditions on an interface of arbitrary shape whose position is itself an unknown is a non-trivial numerical problem. A wide range of methods have been developed in the case of Newtonian fluids, but the extension of these methods to non-Newtonian rheologies is a topic of active research (Vola *et al.* 2004; Chauchat & Médale 2010). In the case of the $\mu(I)$ -rheology in more than one dimension, the coupling between the rheology (which is pressure-dependent) and the free-surface boundary conditions makes the problem more difficult. This has hampered previous efforts of implementation (Pouliquen & Forterre 2009; Cawthorn 2011).

Considering an interface rather than a free surface simplifies a number of numerical details. In particular, the continuity of the velocity field through the interface is guaranteed and simple (but approximate) techniques are available to evaluate viscous stresses at the interface. This treatment of interfaces and viscous terms within Gerris has been validated extensively using thorough test cases and applications to difficult problems (Popinet 2009; Bagué *et al.* 2010). The extension of this method to the $\mu(I)$ -rheology is straightforward. We will show that it leads to accurate results for simple test cases and allows the treatment of complex problems with large interface deformations (and possibly merging and breakup of interfaces).

2.3. Validation for avalanching dry granular flows

2.3.1. Single-layer case, analytical solution

We first consider a two-dimensional granular flow along an inclined infinite plane. This case was studied by Bagnold (1954) using a simple model. The tilt angle is α , x is the direction along the plane and y is the perpendicular direction (figure 1). The flow is supposed steady and incompressible. We assume that we can use the formulation of continuum mechanics. In a pure fluid picture, the stress tensor is decomposed into two contributions, $\sigma_{xy} = \tau$ and $\sigma_{yy} = -p$, respectively, tangential and normal to the flow. There is no constraint at the top of the layer: $\tau = 0$ and $p = 0$ at $y = H$, where H is the thickness of the granular layer ($d \ll H$, where d is the grain diameter). We assume a no-slip condition at the bottom (i.e. at $y = 0$). The conservation of mass is consistent with the velocity field, so that $u = u(y)$ and $v = 0$, where u and v are the components of the velocity field in the x and y directions, respectively. Under these hypotheses, the conservation of momentum implies the following equilibrium between stress and weight:

$$0 = \frac{\partial}{\partial y}\tau + \rho g \sin \alpha \quad \text{and} \quad 0 = -\frac{\partial}{\partial y}p - \rho g \cos \alpha, \quad (2.19)$$

where ρ is the density of the grains. These conservation equations can be integrated once without assumptions on the constitutive law. There is no constraint at the top of the layer: $\tau = 0$ and $p = 0$ at $y = H$. So that we have, for any rheology,

$$\tau = \rho g H \left(1 - \frac{y}{H}\right) \sin \alpha \quad \text{and} \quad p = \rho g H \left(1 - \frac{y}{H}\right) \cos \alpha. \quad (2.20)$$

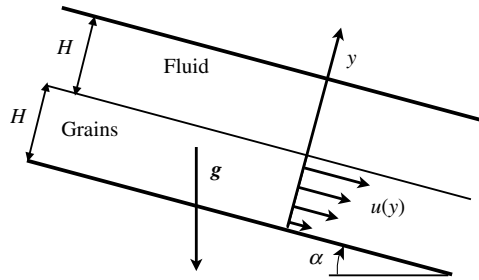


FIGURE 1. Sketch of the granular material moving along a flat rigid bed inclined at an angle α ; the coordinate x is along the slope, and y is the coordinate normal to the plane. The bottom is at $y = 0$, and the top is at $y = 2H$. The thickness of the flow is H (much larger than the grain size, $d \ll H$). The flow is parallel to the slope $u = u(y)$ and $v = 0$. In § 2.3.3 the granular medium is covered by a fluid, and there is an interface at $y = H$ and a rigid wall at $y = 2H$, thus forming a channel.

We can here introduce the Bagnold viscosity prior to the $\mu(I)$ -viscosity. From his observations, Bagnold (1954) derived a simple rheology in which the granular flow behaves as a viscous flow obeying

$$\tau = \rho v \frac{\partial u}{\partial y}, \tag{2.21}$$

where $\eta = \rho v$ is a kinematic viscosity, and v can be constructed with local quantities, such as the grain size d and the shear rate (note that, in the following, we use the notation η for the dynamic viscosity to avoid confusion with the friction coefficient μ of the granular rheology). In the case of a parallel sheared flow,

$$v = d^2 \frac{\partial u}{\partial y} \tag{2.22}$$

is a good candidate, if only from dimensional analysis. We deliberately choose a unit constant of proportionality for the sake of simplicity.

This formulation is reminiscent of the Prandtl turbulent viscosity (Schlichting 1987). Using relation (2.22), the conservation of momentum gives the following solution for the velocity, known as the Bagnold velocity profile:

$$\left. \begin{aligned} u &= \frac{2}{3} \sqrt{gd} \left(\sin \alpha \frac{H^3}{d^3} \right)^{1/2} \left[1 - \left(1 - \frac{y}{H} \right)^{3/2} \right], & v &= 0, \\ p &= \rho g H \left(1 - \frac{y}{H} \right) \cos \alpha. \end{aligned} \right\} \tag{2.23}$$

In fact, many authors call Bagnold profile the dependence $[1 - (1 - (y/H))^{3/2}]$ itself. One obvious limitation of this model is that, for any value of the slope angle α , no matter how small, the velocity is non-zero and a flow develops; in other words, Bagnold's model does not take into account the existence of a critical angle of avalanche below which there is no flow.

We now turn to the $\mu(I)$ model. As above, we consider a two-dimensional steady incompressible granular flow of thickness H along an infinite plane inclined at an angle α . The integrated equilibrium (2.20) gives p and τ as functions of y . By definition, $\mu(I) = \tau/p$; the above expressions for the components of the stress tensor give that μ is constant for a given value of the slope α , that is, $\mu(I) = \tan \alpha$.

This implies that, for a given value of the slope α , the inertial number I is a constant, $I = I_\alpha$, with $I_\alpha = \mu^{-1}(\tan \alpha)$, where μ^{-1} is the inverse of the function μ :

$$\mu^{-1}(\tan \alpha) = I_0 \frac{\tan \alpha - \mu_s}{\mu_s + \Delta\mu - \tan \alpha}. \quad (2.24)$$

From the definition of the inertial number (2.3), we obtain $d(\partial u/\partial y) = I_\alpha \sqrt{\rho/\rho}$. The shear rate is thus an explicit function of y :

$$\frac{\partial u}{\partial y} = \frac{I_\alpha}{d} \sqrt{gH \left(1 - \frac{y}{H}\right) \cos \alpha}, \quad (2.25)$$

which is integrated using the no-slip condition at $y = 0$. This leads, for $\tan \alpha > \mu_s$ and $0 < y < H$, to

$$\left. \begin{aligned} u &= \frac{2}{3} I_\alpha \sqrt{gd \cos \alpha} \frac{H^3}{d^3} \left[1 - \left(1 - \frac{y}{H}\right)^{3/2} \right], & v &= 0, \\ p &= \rho g H \left(1 - \frac{y}{H}\right) \cos \alpha. \end{aligned} \right\} \quad (2.26)$$

We thus recover a Bagnold profile (i.e. $[1 - (1 - (y/H))^{3/2}]$), but with a different prefactor, and a relation expressing hydrostatic balance. The slope angle α now has to be larger than $\arctan(\mu_s)$ to induce a flow, which is consistent with an avalanching threshold.

Note. The ratio $\tau/(\partial u/\partial y)$ defines an equivalent viscosity for the flow; its expression in this case is

$$\rho v_{eq} = \rho(d/H) \frac{\sin \alpha \sqrt{gH} H}{(\cos \alpha)^{1/2} I_\alpha} \sqrt{1 - y/H}, \quad (2.27)$$

so that its value is zero at the surface. At the limit of validity of the continuum mechanics approximation, we can consider that the smallest value taken by the viscosity corresponds to the value at a depth of one grain below the surface: the smallest kinematic viscosity is thus the kinematic viscosity evaluated at $y = H - d$. From relation (2.27),

$$v_{min} \simeq \frac{\sin \alpha \sqrt{gH} H}{(\cos \alpha)^{1/2} I_\alpha} \left(\frac{d}{H}\right)^{3/2}, \quad (2.28)$$

and the order of magnitude of the smallest value of the viscosity is approximately $\rho \sqrt{gd^3}$.

2.3.2. Single-layer case, numerical solution

As explained, we implement the $\mu(I)$ -viscosity (2.18) in the Navier–Stokes solver. The initial velocity profile at $t = 0$ is $u = v = 0$, but in practice we use the Bagnold solution to speed up the computations.

We consider a single granular layer of thickness H (see § 2.3.2). The pressure is imposed at the top of the domain, $p = 0$, as well as the transverse velocity, $v(H) = 0$. The longitudinal velocity follows a Neumann condition $\partial_y u(H) = 0$. The problem is solved on a square grid periodic in x . The equations are solved using non-dimensional variables: $(x, y) = H(\bar{x}, \bar{y})$ for space, $(u, v) = \sqrt{gH}(\bar{u}, \bar{v})$ for velocities,

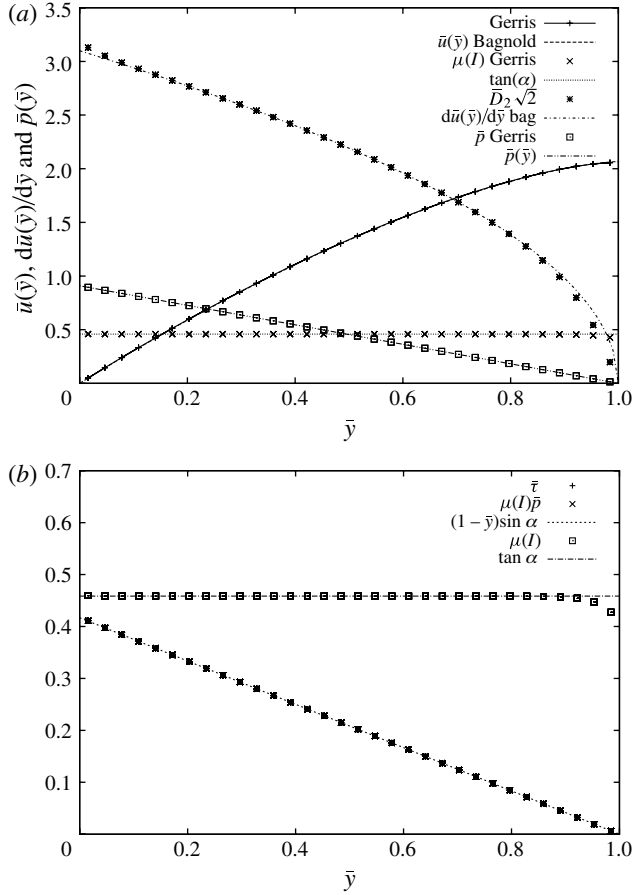


FIGURE 2. Comparison between (a) analytical and (b) computed (on a 32×32 grid) profiles for a single granular layer ($0 < \bar{y} < 1$) with the $\mu(I)$ -rheology. The slope angle is $\alpha = 0.43$, and $\bar{d} = 1/25$. (a) Analytical equation (2.26) and Gerris solution for the pressure, velocity and velocity gradient. (b) Comparison of shear stress $\bar{\tau} = \bar{\eta} d\bar{u}/d\bar{y}$ (+), $\mu(I)\bar{p}$ (x) and exact solution (dashed line); and comparison of the computed $\mu(I)$ (\square) with the exact solution $\tan \alpha$ (dot-dashed line).

and $p = \rho g H \bar{p}$ for pressure. The non-dimensional viscosity is thus $\bar{\eta} = [\mu(I)/\sqrt{2}\bar{D}_2]\bar{p}$ and $I = \bar{d}\sqrt{2}\bar{D}_2/\sqrt{|\bar{p}|}$.

Figure 2 shows an example of solution for the velocity, the velocity gradient and the pressure profiles for a given value of the slope angle $\alpha = 0.43$. We obtain a numerical solution consistent with the analytical solution, within discretization errors. The computed resulting viscous component $\bar{\eta} d\bar{u}/d\bar{y}$ is found to be proportional to \bar{p} , and the coefficient of proportionality remains constant and equal to $\mu(I)$ as expected.

This simulation was repeated using 8, 16, 32 or 64 points across the channel. Figure 3 shows the evolution of the L^2 and max norms of the difference between the computed velocity and the exact Bagnold solution as a function of the number of grid points across the layer. The convergence is intermediate between first and second order in the spatial resolution.

Figure 4 shows the evolution of the velocity at the surface: $u(y = H)$ for both numerical and analytical solutions as a function of slope angle α . The analytical

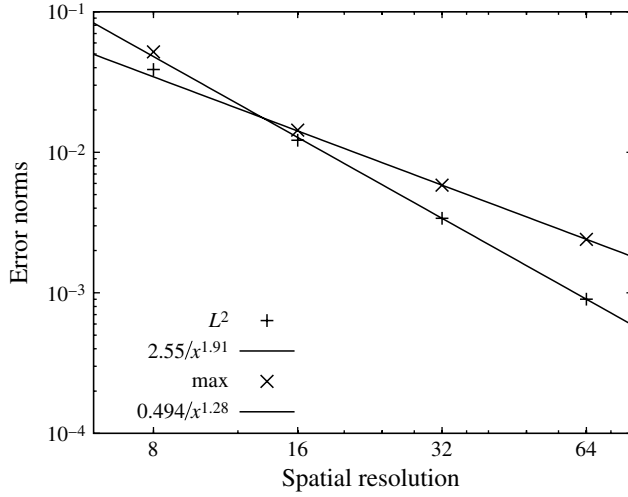


FIGURE 3. Convergence of the error norms of the difference between the computed velocity and the exact Bagnold solution error norms L^2 and max as a function of resolution (number of grid points across the granular layer).

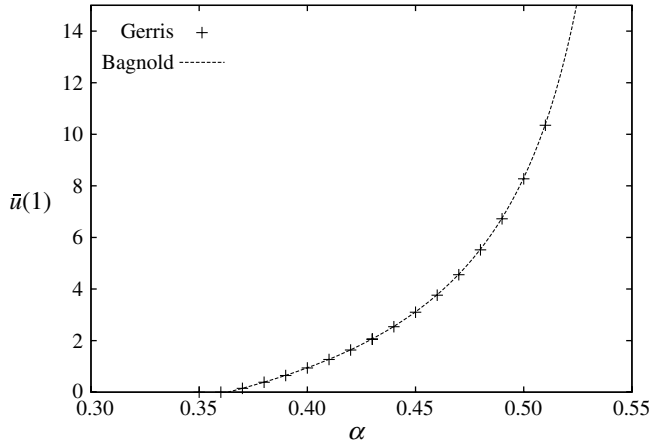


FIGURE 4. In the case of a single granular layer ($0 < \bar{y} < 1$), comparison between numerical (+) and analytical (dashed line) solutions for the velocity at the surface $\bar{u}(\bar{y} = 1)$ as a function of the slope angle α . For $\alpha < \arctan(\mu_s) \simeq 0.363$ there is no motion, as expected.

solution is given by (2.26) and reads $\bar{u}(1) = 2(\sqrt{\cos \alpha} I_\alpha / \bar{d})/3$, with

$$I_\alpha = I_0 \frac{-\mu_s + \tan \alpha}{\mu_s + \Delta\mu - \tan \alpha} = \mu^{-1}(\tan \alpha). \tag{2.29}$$

The agreement between the two solutions is excellent. In particular the numerical method is able to accurately capture the avalanching transition.

2.3.3. *Two-layer case, analytical solution*

The classical $\mu(I)$ model does not take into account the influence of the fluid surrounding the granular medium, assumed to be negligible; indeed, the density of

glass beads is 2500 kg m^{-3} , the density of sand is just less than 2000 kg m^{-3} , whereas the density of air is 1.2 kg m^{-3} . This is justified by the fact that experiments show that dry granular flows are not affected by the surrounding air. We place ourselves in this case, and directly solve the flow of a dry granular layer overlaid with a Newtonian fluid. In the limit of a light enough overlying fluid, the pressure at the top of the granular medium will be close to zero. We insist that underwater avalanches would require a different formulation, and take into account at least a two-phase mixture in the bottom and more complex modelling (Cassar, Nicolas & Pouliquen 2005; Pailha & Pouliquen 2009; Chauchat & Médale 2010), which is not within the scope of the present analysis.

To recover the solution for a pure free surface, one has to be careful, however. The viscosity of the overlying fluid must remain small enough to prevent any shear perturbation of the granular flow. On the other hand, if the fluid is too light and not viscous enough, numerical problems may arise. We thus consider a granular layer overlaid with a Newtonian fluid of viscosity $\eta_f = \rho_f \nu_f$ and density ρ_f , and separated by an interface at $y = H$. The problem consists of solving the continuity equations for each of the two layers.

For the upper fluid ($H < y < 2H$), the conservation of momentum gives simply

$$0 = \frac{\partial}{\partial y} \left(\eta_f \frac{\partial u}{\partial y} \right) + \rho_f g \sin \alpha \quad \text{and} \quad 0 = -\frac{\partial}{\partial y} p - \rho_f g \cos \alpha, \quad (2.30)$$

with a no-slip condition at the upper wall: $u(2H) = 0$. We arbitrarily set $p = 0$ at $y = 2H$. We thus obtain

$$u(y) = \frac{(2H - y)(\rho_f g y \sin \alpha - 2\tau_0)}{2\eta_f} \quad \text{and} \quad p(y) = \rho_f g H \left(2 - \frac{y}{H} \right) \cos \alpha. \quad (2.31)$$

At the interface, $p(H) = \rho_f g H \cos \alpha$; the stress components are thus $p_0 = \rho_f g H \cos \alpha$ and $\tau_0 = \eta_f u'(H)$. We solve for the granular layer ($0 < y < H$) using the $\mu(I)$ -rheology. Using the equality of constraints at $y = H$, we introduce τ_0 and p_0 as constants of integration for the balance equations (2.19) (thus obtaining $p = p_0 + \rho g H \cos \alpha (1 - y/H)$ and $\tau = \tau_0 + \rho g H \sin \alpha (1 - y/H)$). By definition, $\mu(I) = \tau/p$, so that the expression for I is deduced by inversion of (2.24). Since $\partial u/\partial y = 0$ when there is no flow:

$$d \frac{\partial u}{\partial y} = \max \left[\sqrt{\frac{p_0}{\rho} + gH \left(1 - \frac{y}{H} \right) \cos \alpha} \mu^{-1} \left(\frac{\tau_0 + \rho g H (1 - y/H) \sin \alpha}{p_0 + \rho g H (1 - y/H) \cos \alpha} \right), 0 \right]. \quad (2.32)$$

By integration, using no-slip condition $u(0) = 0$ and the continuity of the velocity at the interface, $u(H^-) = u(H^+)$, we obtain the velocity profile. In practice, we solve two ordinary differential equations (ODEs) (using a shooting method with Runge–Kutta differentiation), and we determine using Newton iterations the value of τ_0 that allows the velocity profiles in $0 < y < H$ and in $H < y < 2H$ to satisfy the condition $u(H^-) - u(H^+) = 0$.

2.3.4. Two-layer case, numerical solution

In this second instance, a VOF tracer c is introduced to discriminate between the granular layer and the overlying Newtonian fluid: $c = 1$ in the granular layer and $c = 0$ in the Newtonian layer. The same periodic condition in x , and a no-slip velocity condition at the bottom of the domain, $\bar{u} = \bar{v} = 0$, are imposed. In addition, a no-slip condition is imposed at the top of the domain, $\bar{u} = \bar{v} = 0$, as well as the pressure $\bar{p} = 0$.

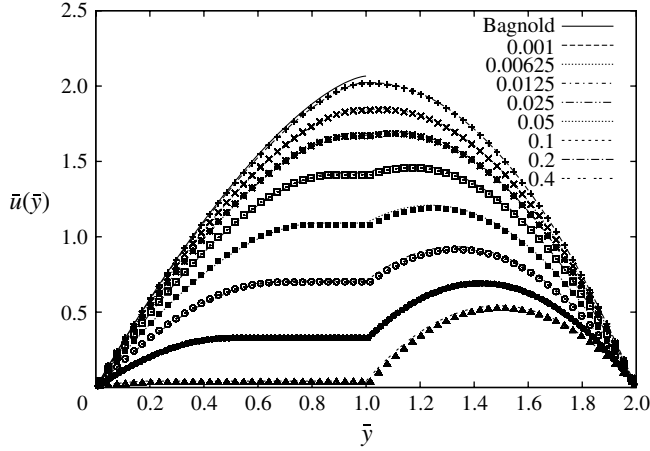


FIGURE 5. Comparison of the Gerris numerical solution (symbols) and the solution of the system of ODEs (2.32) corresponding to the case of two (phases) layers (lines), for $v_f/\sqrt{gH^3} = 0.1$ and different values of the density ratio ρ_f/ρ from 0.001 to 0.4 (large values have no physical application but validate the numerics). The slope is $\alpha = 0.43$. The corresponding Bagnold profile is plotted with a solid line for $0 < \bar{y} < 1$.

The initial velocity profile at $t = 0$ is $u = v = 0$, but in practice we use the Bagnold solution and a linear profile for $2H > y > H$ to speed up the computations. The density is scaled by ρ and we use $\eta_f/(\rho\sqrt{gH^3})$ as viscous parameter.

In this (more challenging) case the interface between the two layers is described using the VOF method of the Gerris solver. The interface is stable and remains at its initial position $y = H$. Figure 5 shows the numerical solution for the two layers (granular and Newtonian), with different values for the density and viscosity of the Newtonian fluid. The overall agreement between the semi-analytical and the numerical solutions is again very satisfying. Gerris computations match the semi-analytical solutions, with lighter and less viscous overlying fluids allowing convergence towards the free-surface Bagnold solution for the underlying granular layer. The amount of deceleration of the granular flow may be computed exactly from the two-layer equations system, but an estimate is sufficient for practical purposes.

Starting from a linear development at small $\tau_0/\rho gH$, we use the formula (2.32) but neglect the influence of the pressure p_0 (which could be reintroduced for a more refined estimate):

$$\begin{aligned} d\frac{\partial u}{\partial y} &\simeq \sqrt{\rho gH \left(1 - \frac{y}{H}\right)} \cos \alpha \mu^{-1} (\tan \alpha) \\ &+ \frac{d\mu^{-1}}{dt} (\tan \alpha) \left(\frac{\tau_0}{\rho gH(1 - y/H) \cos \alpha} \right). \end{aligned} \quad (2.33)$$

After integration, this gives a first-order estimate for the variation of the velocity at the top of the layer:

$$\frac{\Delta u}{u(H)} = -\frac{3\Delta\mu}{\cos \alpha(\mu_s - \tan \alpha)(\Delta\mu + \mu_s - \tan \alpha)} \frac{\tau_0}{\rho gH} + O\left(\left(\frac{\tau_0}{\rho gH}\right)^2\right). \quad (2.34)$$

This variation is linked to the viscosity of the granular layer ν_{eq} ; however, τ_0 depends on the upper fluid characteristics. If its density ρ_f is large, the fluid is flowing in response to its weight, $\tau_0 \sim \rho_f g H \sin \alpha$. In that case, the velocity of the granular layer at the interface being $\sqrt{gH} H/d$, the error estimate is

$$\frac{\Delta u}{\sqrt{gH} H/d} \simeq \frac{\rho_f}{\rho}. \quad (2.35)$$

Conversely, if its density is small, the upper fluid is dragged by the granular layer and its velocity reaches close to $\sqrt{gH} H/d$. In that case, the error estimate is

$$\frac{\Delta u}{\sqrt{gH} H/d} \simeq \frac{\eta_f}{\rho \sqrt{gH} d}. \quad (2.36)$$

These estimates are useful to evaluate *a priori* the influence of the Newtonian layer. Note that the avalanching configuration addressed in this section maximizes this influence as the upper layer of Newtonian fluid takes much more time to reach a stationary regime than the granular layer does, thus implying a long total simulation duration.

In this section, numerical results compare well with analytical solutions with one or two layers. We are also able to estimate the order of magnitude of the departure from the free-surface solution as a function of density and viscosity ratios. We expect that the influence of the external Newtonian fluid will be smaller in the case of fast transient events than for the stationary two-layer problem considered in this section. So, we now turn to a more challenging and interesting case: the collapse of granular columns. This will involve the unsteady and convective derivative terms in the Navier–Stokes resolution, all the spatial derivatives, complex interface/free-surface deformation as well as the rheological model itself.

3. The granular column collapse as a continuum

3.1. The collapse experiment from grains to continuum

3.1.1. Experimental scalings in two dimensions

The granular column collapse experiment consists of allowing an initially confined column of grains to collapse onto a horizontal plane under its own weight. The subsequent flow starts with a vertical fall combined with lateral spreading, followed by the advance, and eventually the arrest, of a granular flow front. The experiment was performed either in axisymmetric configurations (Lajeunesse *et al.* 2004; Lube *et al.* 2004) or in quasi two dimensions, namely using a planar Hele-Shaw cell (Lajeunesse, Monnier & Homsy 2005; Lube *et al.* 2005; Lacaze, Phillips & Kerswell 2008). A three-dimensional investigation (namely, planar with varying confinements) was performed by Balmforth & Kerswell (2005). In all configurations, the material was released by opening a swinging gate or by swiftly pulling up the container. The focus was set on the scaling law obeyed by the run-out, that is, the final distance covered by the flow front. If the initial height of the column is H_0 , its initial half-width is L_0 , the final maximum thickness is H_∞ and the final half-width is L_∞ (see figure 6 for a schematic illustration), the experimental scaling for the run-out in the planar two-dimensional configuration reads:

$$\frac{L_\infty - L_0}{L_0} \simeq \begin{cases} \lambda_1 a, & a < a_0, \\ \lambda_2 a^\alpha, & a > a_0, \end{cases} \quad (3.1)$$

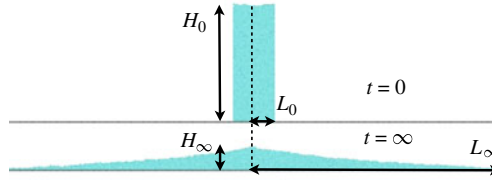


FIGURE 6. (Colour online available at journals.cambridge.org/flm) Schematic illustration of the column collapse experiment in two dimensions. The initial height of the column is H_0 , its initial half-width is L_0 and $a = H_0/L_0$ is the aspect ratio; the final maximum thickness is H_∞ and the final half-width, or run-out, is L_∞ .

where $a = H_0/L_0$ is the column aspect ratio, and a_0 , λ_1 and λ_2 are essentially material-dependent parameters. Lube *et al.* (2005) found $\lambda_1 \simeq 1.2$, $\lambda_2 \simeq 1.9$ and $1.8 \leq a_0 \leq 2.8$ for sand, rice and sugar, while Lajeunesse *et al.* (2005) found $\lambda_1 \simeq 1.8$, $\lambda_2 \simeq 2.3$ and $a_0 \simeq 3.0$ for glass beads. The exponent α is close to $2/3$ in all experiments.

Similar scaling was obtained for the final height of the deposit:

$$\frac{H_\infty}{L_0} \simeq \begin{cases} \lambda_3 a, & a < a_0, \\ \lambda_4 a^\alpha, & a > a_0, \end{cases} \quad (3.2)$$

where Lube *et al.* (2005) found $\lambda_3 \simeq 1.0$, $\lambda_4 \simeq 1$, $a_0 \simeq 1.15$ and an exponent $\alpha = 0.4$, while Lajeunesse *et al.* (2005) found $\lambda_3 \simeq 1.0$, $\lambda_4 \simeq 0.9$, $a_0 \simeq 0.7$ and an exponent $\alpha \simeq 1/3$.

3.1.2. Numerical granular collapse

Two-dimensional numerical simulations of the column collapse were performed using discrete methods, namely solving individual grain trajectories taking into account interactions with neighbours while neglecting the influence of the surrounding air and of confining walls (Zenit 2005; Staron & Hinch 2005, 2007; Lacaze *et al.* 2008). They proved successful in reproducing the scaling laws observed experimentally, thus showing the negligible role of the interaction between grains and air compared to the grain-to-grain interactions. Moreover, Lacaze *et al.* (2008) showed that discrete simulations reproduce very accurately experimental results in two dimensions, down to the grain size scale. Applying a contact dynamics method (Moreau 1994), Staron & Hinch (2005) recovered scaling (3.1) with an exponent of 0.7 and $\lambda_1 \simeq 2.5$, $\lambda_2 \simeq 3.25$ and $a_0 \simeq 2$, and scaling (3.2) with $\lambda_3 \simeq 1$, $\lambda_4 \simeq 0.65$, $a_0 \simeq 1$ and an exponent $\alpha = 0.35$, although a third regime ($H_\infty/L_0 = 1.45$) was also observed for $a \gtrsim 10$.

Discrete numerical simulations are a powerful tool to explore the internal structure of the flow and its dynamics. In the following, we apply a contact dynamics algorithm to simulate the collapse of granular columns in two dimensions. This method assumes perfectly rigid grains obeying the standard Newtonian equations of motion. The grains interact at contacts through a Coulombic friction law involving a single parameter, the contact coefficient of friction μ . In addition, a coefficient of restitution e sets the energy dissipated in the advent of a collision. More details on the method can be found in Moreau (1994).

Using two-dimensional circular grains of mean diameter d , we simulate the collapse of columns with aspect ratios $a = 0.5$, $a = 1.42$ and $a = 6.26$, containing 3407, 6041 and 6036 grains, respectively. We have also explored the extreme case of a column with $a = 67.9$ containing 20050 grains. Contact parameters are $\mu = 0.5$ and $e = 0.5$; these values were not varied. The simulation protocol is exactly that described in

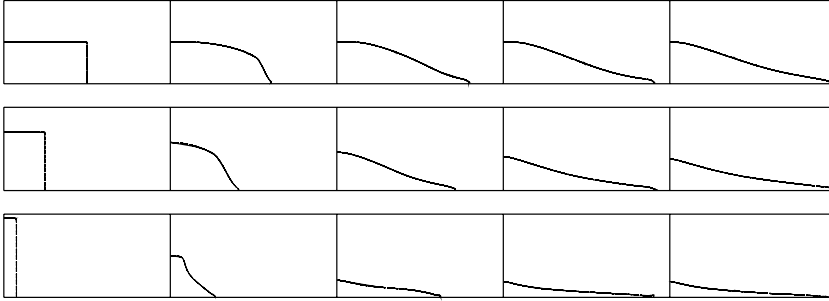


FIGURE 7. Strip representing a series of snapshots of a column collapse with aspect ratio $a = 0.5, 1.42, 6.26$ (from top to bottom) simulated with Gerris at time $\bar{t} = 0, 1, 2, 3, 4$. The surrounding fluid is Newtonian of density ρ_f and viscosity η_f , while the non-Newtonian $\mu(I)$ -rheology is used for the column.

Staron & Hinch (2007): the column of grains is prepared by random deposition under gravity, and is allowed to collapse at $t = 0$ onto a horizontal plane made rough by gluing grains on its surface. In the following, trusting that discrete simulations accurately reproduce the phenomenology of the granular column collapse, contact dynamics simulations are used for systematic comparison with the continuum model using the Gerris flow solver, in which the $\mu(I)$ -rheology (as well as others) was implemented as explained in § 2.2.

3.1.3. The Gerris collapse in two dimensions

The Navier–Stokes equations are non-dimensionalized using the characteristic length H_0 (the initial column height), characteristic velocity $\sqrt{gH_0}$ and characteristic time $\sqrt{H_0/g}$. The continuum simulation of the granular collapse consists of allowing a column of fluid obeying the non-Newtonian $\mu(I)$ -rheology to collapse in response to gravity onto a horizontal plane. The column is surrounded by a light fluid of density $\bar{\rho}_f = 10^{-3}$ (normalized by ρ_{grains}) and viscosity $\bar{\eta}_f = 10^{-4}$ (normalized by $g^{1/2}L_0^{3/2}\rho_{grains}$). Rather than imposing a zero-pressure condition at the top of the simulation cell, we impose $p = -\rho_f\ell$, where ℓ is the size of the computation domain. Doing so, the pressure at the top of the granular layer is close to zero, and is actually zero at the very front of the flow. We find, however, that this correction has a very small influence for $\bar{\rho}_f = 10^{-3}$. A no-slip condition is implemented at the bottom, while a slip (symmetry) condition is imposed on the left wall of the simulation cell. The quadtree spatial discretization used in Gerris allows for efficient adaptive mesh refinement. This is used in this study to refine the mesh within the granular material. A coarse mesh is used to discretize the surrounding Newtonian fluid far enough from the interface with the granular flow. This allows one to limit confinement effects by using a very large domain ($\ell/L_0 \approx 64$) at a negligible computational cost. In all the results presented, care was taken to ensure grid independence (the typical spatial resolution within the granular material is of order $L_0/\Delta x = 32$). For illustration, series of snapshots for $a = 0.5$, $a = 1.42$ and $a = 6.26$ showing the initial state and the collapse at $\bar{t} = t/(H_0/g)^{1/2} = 0, 1, 2, 3, 4$ are displayed in figure 7.

3.2. Comparing scalings and dynamics

3.2.1. Shape and inner deformation

Applying the contact dynamics method, we have simulated the collapse of granular columns with $a = 0.5$, $a = 1.42$ and $a = 6.26$. In order to highlight the deformations

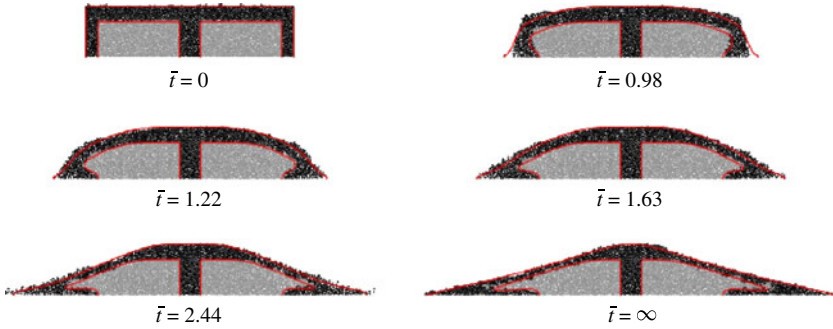


FIGURE 8. Comparison between the $\mu(I)$ continuum model (red line) and contact dynamics simulations (grains) for an aspect ratio $a = 0.5$ at different times (non-dimensionalized by $\sqrt{H_0/g}$). The grains are coloured in the initial heap, which allows one to track the displacement (see Staron & Hinch 2005). The parameters of the $\mu(I)$ -rheology are $\mu_s = 0.32$, $\Delta\mu = 0.28$ and $I_0 = 0.4$.

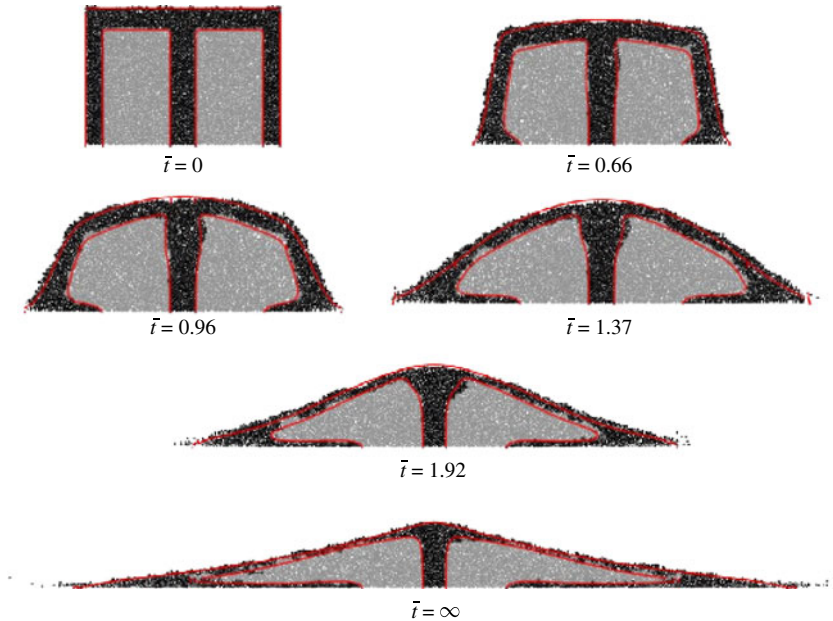


FIGURE 9. Comparison between the $\mu(I)$ continuum model (red line) and contact dynamics simulations (grains) for an aspect ratio $a = 1.42$ at different times (non-dimensionalized by $\sqrt{H_0/g}$). The parameters of the $\mu(I)$ -rheology are $\mu_s = 0.32$, $\Delta\mu = 0.28$ and $I_0 = 0.4$.

occurring in the bulk of the flow, grains at the periphery and in the centre were initially coloured in black and act as tracers. For the same values of aspect ratios, continuum simulations applying Garris and the $\mu(I)$ -rheology were performed. For all three cases, the value of the rheological parameters is the same, namely $\mu_s = 0.32$, $\Delta\mu = 0.28$ and $I_0 = 0.4$. Systematic comparison with discrete simulations was carried out; the results are displayed in figures 8–10. The continuum simulations are represented by two red lines showing the time evolution of the shape of the outline as well as the shape of the inner volume. We observe that in all cases the agreement

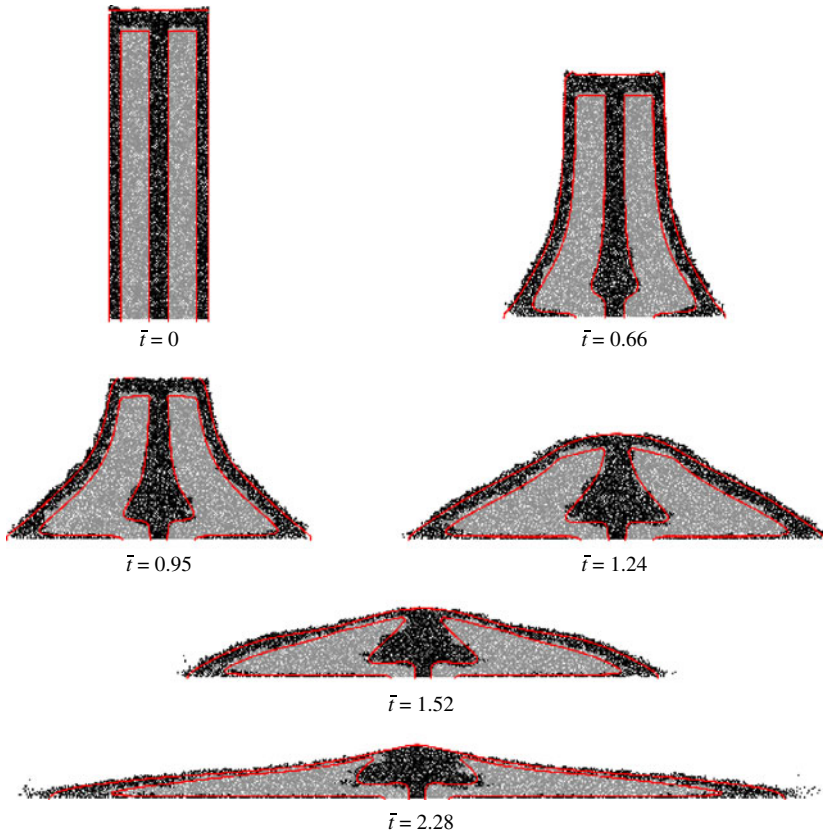


FIGURE 10. Comparison between the $\mu(I)$ continuum model (red line) and contact dynamics simulations (grains) for an aspect ratio $a = 6.26$ at different times (non-dimensionalized by $\sqrt{H_0/g}$). The parameters of the $\mu(I)$ -rheology are $\mu_s = 0.32$, $\Delta\mu = 0.28$ and $I_0 = 0.4$.

between continuum and discrete simulations is good: both the outer shape and the inner deformations are well predicted by the continuum model. This is particularly visible in the case of the tall column ($a = 6.26$, figure 10), where an inner triangular-shaped area develops at the base of the falling edifice. As can be seen in figure 10, however, the head of the front when close to arrest reduces to a few grain diameters. Continuum simulation of such a thin granular layer is expected to be problematic. The following subsection deals with this issue.

3.2.2. Propagation of the flow front

In two-dimensional discrete simulations, the position of the flow front in the course of time is defined by the last grain(s) flowing at the foot of the flow, but still touching the bulk: any grain rolling free ahead is not considered. This criterion is difficult to apply in practice, as the front looks like a cloud of colliding grains rather than a dense flow of contacting spheres. Hence, we have determined the position of the granular front in the course of time by analysing the shape of the falling edifice and by identifying the position where the outline reaches a zero height, discarding all grains bouncing beyond (as an illustration, figure 18 shows the front of the collapsing column for $a = 6.26$ at $\bar{t} = 1.33$, 2.0 and 2.66).

In the case of the continuum model, the flow front is defined by the position of the contact point on the bottom plane of the interface between the granular continuum and

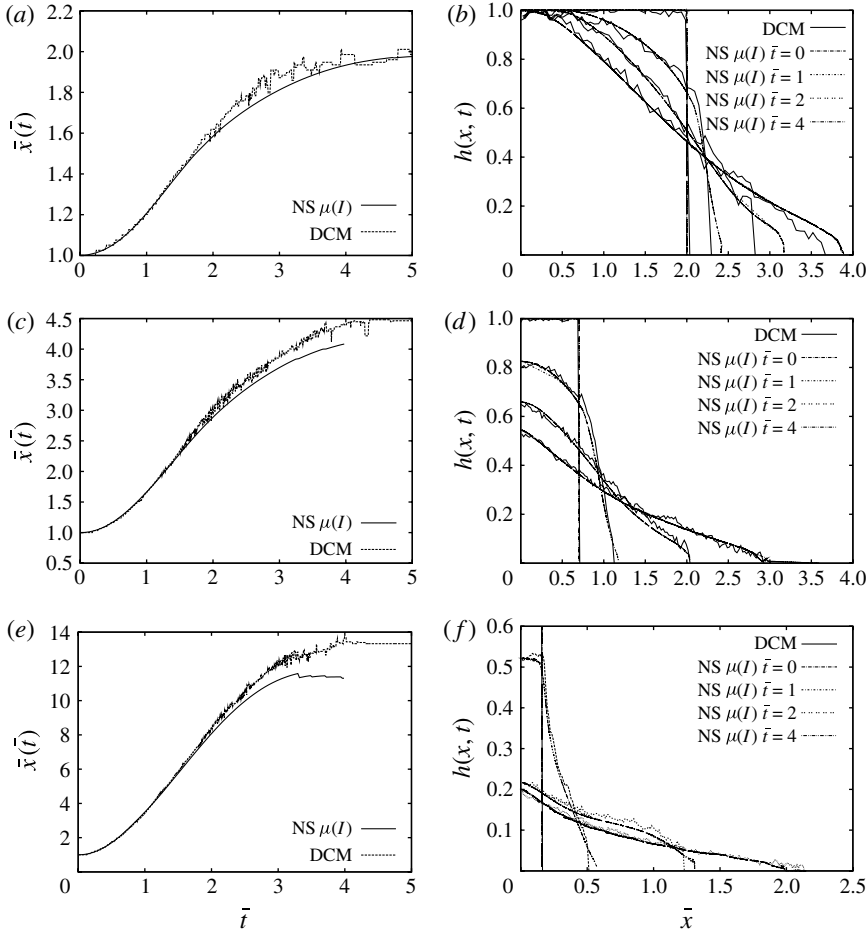


FIGURE 11. Normalized position of the flow front x/L_0 as a function of the normalized time $\bar{t} = t/(H_0/g)^{1/2}$ and height profiles at different instants $t\sqrt{g/H_0} = 0, 1, 2$ and 4 , in the case of columns of aspect ratios (a,b) $a = 0.5$, (c,d) $a = 1.42$ and (e,f) $a = 6.26$, for discrete contact dynamics simulation (noisy dashed line) and continuum Gerris simulation with the $\mu(I)$ -rheology (plain line).

the surrounding fluid. This is in fact a ‘moving contact line’ problem, which presents difficulties of its own. Although this position is usually well defined, ‘droplets’ of granular material can sometimes detach from the bulk near the foot of the avalanche, thus offering an interesting analogue with detaching grains in the discrete version. These droplets are, however, largely an artefact of the numerical treatment of the moving contact line problem (their diameter is typically comparable to the grid size). They are ignored when estimating the position of the front. Care was taken in all cases to ensure that the flow front position was independent of grid size (so that possible numerical artefacts linked to the treatment of the moving contact line did not affect the results).

For the three cases $a = 0.5$, $a = 1.42$ and $a = 6.26$, we have reported the position of the flow front in the course of time for discrete and continuum simulations, as well as height profiles at different instants of the collapse (figure 11). In all three cases, the front propagation in the first part of the granular collapse (corresponding to

the acceleration phase, namely $\bar{t} \lesssim 2$) is well captured by the continuum simulations. When the flow starts decelerating, however, the continuum simulations slow down earlier than discrete granular flows, and systematically underestimate the run-out, i.e. the front final position. The error is larger for larger aspect ratios (reaching 10%) and coincides with the final part of the granular deposit formed by a thin layer of a few grains in height, where the assumption of a continuum is questionable. This aspect is further discussed in §4.3. Furthermore, we see for example on figure 11(e) that the position of the front computed by Gerris may slightly decrease owing to the ejection of droplets mentioned in the previous paragraph. In spite of this, the correct description of the front propagation at earlier stages, as well as the recovery of the bulk shape evolution in the course of time, support the ability of a continuum Navier–Stokes approach with a $\mu(I)$ -rheology to reproduce correctly the granular collapse and the subsequent flow.

3.2.3. Scaling for the run-out for the continuum $\mu(I)$ -rheology

The main outcome of the granular column collapse experiment is the scaling relationship obtained for the run-out (see §3.1.1): $(L_\infty - L_0)/L_0 \propto a$ for $a < a_0$ and $(L_\infty - L_0)/L_0 \propto a^{2/3}$ otherwise.

Applying Gerris with the $\mu(I)$ -rheology, we have carried out collapse experiments with values of aspect ratio a ranging between 0.25 and 64. To check the grid independence of the results, the spatial resolution was varied from $L_0/\Delta x = 16$ (nine levels of refinement) to $L_0/\Delta x = 128$ (12 levels of refinement). The run-out distance L_∞ was measured, and the normalized run-out $(L_\infty - L_0)/L_0$ plotted as a function of the aspect ratio a (figure 12a). In agreement with experimental results in two dimensions, we observe the existence of a linear regime for smaller a , followed by a power-law regime with an exponent $\alpha = 0.7$ for larger a . The scaling obtained reads:

$$\frac{L_\infty - L_0}{L_0} \simeq \begin{cases} 2.2a, & a \lesssim 7, \\ 3.9a^{0.7}, & a \gtrsim 7. \end{cases} \quad (3.3)$$

Note that both regimes are closely approximated by power laws. The exponents obtained are within the error bars of the exponents obtained using contact dynamics simulations or experiments (which typically display a much larger scatter of run-out values). Only the value of the aspect ratio a_0 characterizing the transition between these two regimes differs from previous observations: we obtain $a_0 \simeq 7$ instead of the experimentally observed $1.8 \lesssim a_0 \lesssim 4$ (Lajeunesse *et al.* 2005; Lube *et al.* 2005), and the numerically observed $a_0 \simeq 2$ (Staron & Hinch 2005). The origin of this discrepancy is not obvious. However, the general agreement in the time evolution of the shape and inner deformation observed in figures 8–10 when comparing continuum and discrete simulations suggests that this difference may result from the underestimation of the run-out by Gerris, rather than from a difference in the bulk dynamics.

3.2.4. Scaling for the final height

Considering the same set of continuum simulations as reported in figure 12(a), we give the normalized final height H_∞/L_0 as a function of the aspect ratio a in figure 12(b). The following scaling is observed:

$$\frac{H_\infty}{L_0} \simeq \begin{cases} a, & a \lesssim 0.5, \\ 0.67a^{0.4}, & 0.5 \lesssim a \lesssim 6, \\ 1.4, & 6 \lesssim a. \end{cases} \quad (3.4)$$

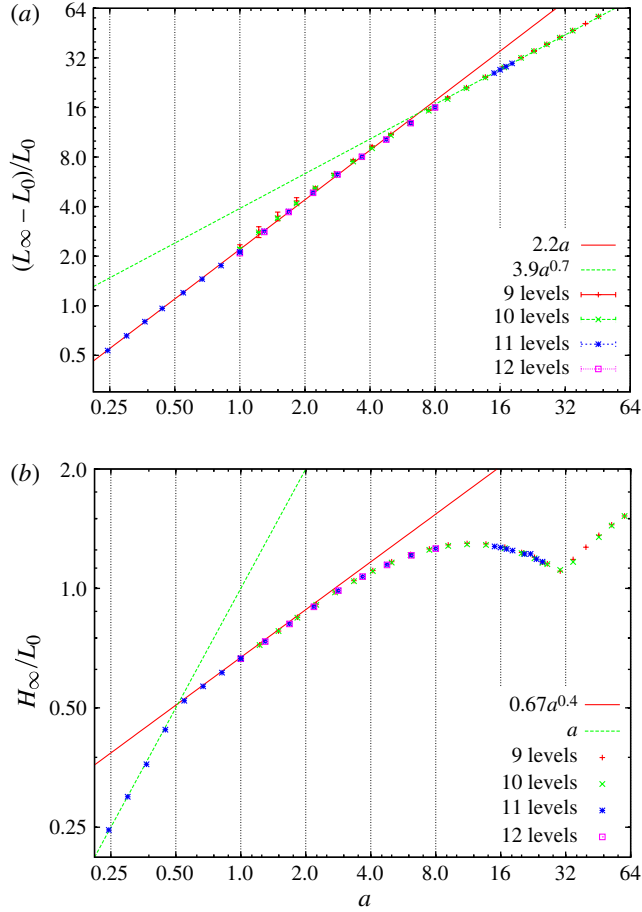


FIGURE 12. (Colour online) (a) Normalized run-out $(L_\infty - L_0)/L_0$ and (b) normalized final height H_∞/L_0 as functions of the aspect ratio a for $\mu(I)$ continuum simulations. The different sets of symbols correspond to increasing spatial resolutions.

The agreement with experimental observations in two dimensions is very good for $a \lesssim 6$ (Lajeunesse *et al.* 2005). For $a \gtrsim 6$, we observe a deviation from the power-law regime to a constant regime, as observed numerically in Staron & Hinch (2005). The appearance of such a plateau is also visible in Lajeunesse *et al.* (2005) (although not interpreted as such) and even in Lajeunesse *et al.* (2006) for Martian data. For larger values of a , H_∞/L_0 decreases, which coincides with the formation of a ‘side bump’. This side bump is initially thinner than the central part of the deposit (for $12 < a < 32$) but becomes thicker when $a > 32$, which explains the increase in the maximum thickness for large aspect ratios. No experimental data are available for comparison in this range of aspect ratios.

3.2.5. Sideways propagation of a bump: the case of $a = 67.9$

In the case of high aspect ratios, the falling material propagates sideways with increasing energy, thus forming a bump and leading to a ‘Mexican hat’ shaped deposit, as described by Lajeunesse *et al.* (2004). To test the ability of the continuum Gerris simulations to reproduce the formation and propagation of this bump, we have

simulated a column collapse with aspect ratio $a = 67.9$, and compared the outcome with a granular contact dynamics simulation. The result is displayed in figure 13. We observe that the evolution of the flow shape obtained with contact dynamics simulations is well reproduced by the continuum simulation. The formation and sideways propagation of the bump is accurate. Moreover, the default set of parameters used for the lower aspect ratios presented earlier also gives a sensible solution for this extreme case (curve in cyan in figure 13). As was the case for lower aspect ratios, the continuum simulation systematically underestimates the flow front position, however.

4. Discussion

4.1. What of other formulations?

As seen in the previous section, the $\mu(I)$ -rheology allows for the recovery of most of the granular column collapse dynamics. For completeness, the results need be confronted to the performance of other plausible candidate rheologies for granular flows. In the following, we successively explore the Newtonian Navier–Stokes model, the Bingham model, the Bagnold model and the constant friction model, all implemented in the Gerris flow solver. Solutions are presented for simple visual inspection on figure 14.

4.1.1. Newtonian Navier–Stokes

For reference, the Newtonian Navier–Stokes case is illustrated in figure 14(b). The flow tends to evolve towards a quasi-uniform thickness, which results in a very different flow front shape compared to the reference $\mu(I)$ -rheology solution (figure 14a). The flow obviously never stops. Note that there is no surface tension in this computation.

4.1.2. The Bingham model

Bingham fluids are characterized by their ability to resist shear at low stresses, while flowing like Newtonian fluids at higher stresses. The existence of a yield value for the shear stress τ_y is the strongest analogy that Bingham fluids bear with granular flows, which present a frictional yield value separating solid-like behaviour (coinciding with an infinite value of viscosity) from avalanching (when the viscosity is finite) (Dufour & Pijaudier-Cabot 2005). The Bingham rheology is implemented by

$$\eta = \eta_0 + \frac{\tau_y}{\sqrt{2}D_2}, \quad (4.1)$$

and is one of the test cases of the Gerris test suite. Using Gerris, we performed simulations of the column collapse for $a = 1.42$. As previously, at low shear rates the viscosity is capped to η_M . The values taken for the yield stress and the viscosity were $\tau_y = 0.001$ and $\eta_0 = 0.1$. The result is displayed in figure 14(c), where a series of snapshots showing the shape of the column at $\bar{t} = t\sqrt{g/H_0} = 0, 1, 2, 3, 4$ is displayed, together with the result obtained with the $\mu(I)$ -rheology (figure 14a). Not surprisingly, the agreement with the experimental granular collapse is poor. In particular, the existence of a yield stress τ_y is responsible for the creation of a solid-like corner advected by the flow, which modifies the final shape of the deposit. When the flow comes to rest, the front exhibits a rounded shape very different from the sharp angle of the granular front.

4.1.3. The Bagnold model

As mentioned in § 2, Bagnold (1954) was the first to establish a rheology where the viscosity is defined by $\eta = \rho d^2 \sqrt{2}D_2$. In that case, the existence of a flow threshold

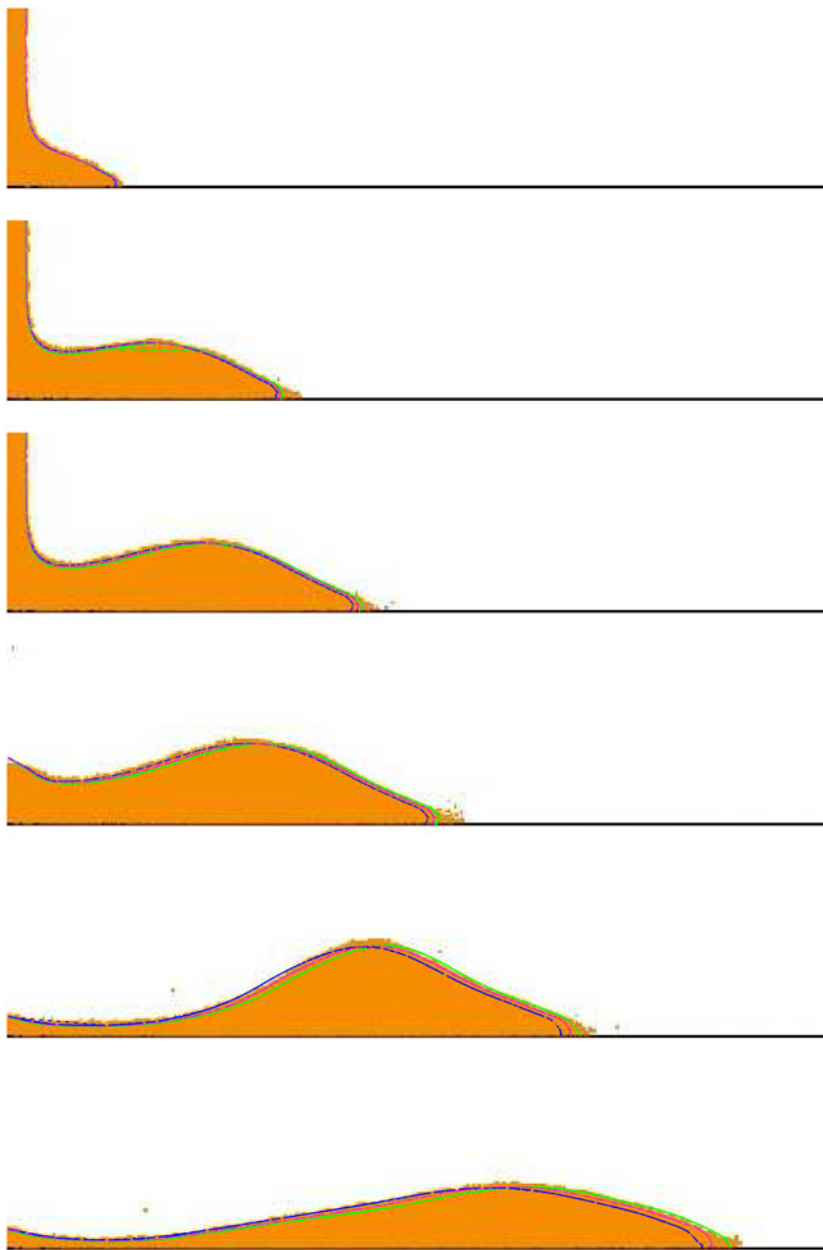


FIGURE 13. A series of snapshots ($\bar{t} = 0.5, 1.0, 1.2, 1.4, 1.7$ and 2.0) of a column collapse with aspect ratio $a = 67.9$ computed by contact dynamics (plain colour) and different values of the $\mu(I)$ -rheology, as an illustration of the sensitivity of the solution to the rheological parameters. The most advanced curve (in green) corresponds to $\mu_s = 0.3$, $\Delta\mu = 0.26$ and $I_0 = 0.30$; the less advanced (in blue), $\mu_s = 0.32$, $\Delta\mu = 0.28$ and $I_0 = 0.30$, fits better the end of the heap. The curve in between (in cyan) corresponds to $\mu_s = 0.32$, $\Delta\mu = 0.28$ and $I_0 = 0.40$ and fits better the top of the surge. This last set of values is the default used throughout this paper.

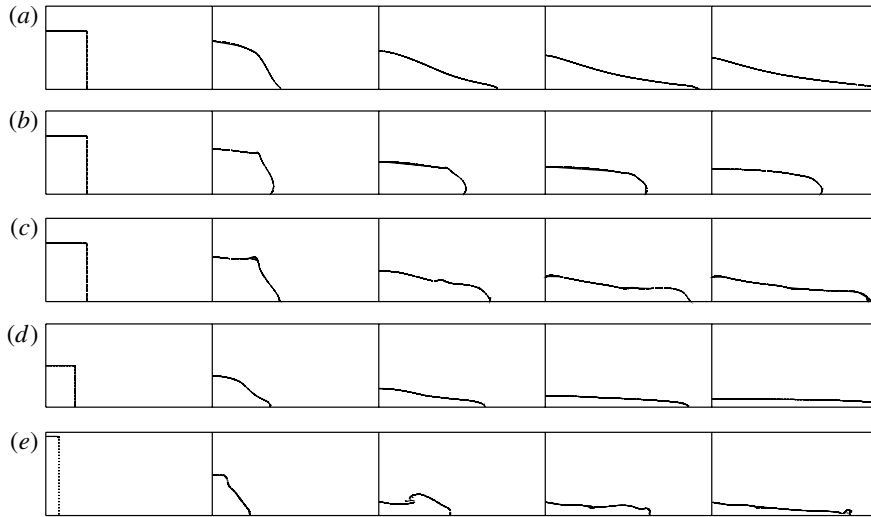


FIGURE 14. Series of snapshots of a column collapse simulated using Gerris with different viscous models (the surrounding fluid is Newtonian of density ρ_f and viscosity η_f): (a) the $\mu(I)$ -rheology with $\mu(I) = 0.3 + 0.26/(0.3/I + 1)$; (b) a simple Newtonian rheology with $\eta_{grains} = 0.1$; (c) a non-Newtonian Bingham rheology with $\eta_{grains} = 0.1/\sqrt{2D_2} + 0.001$; (d) Bagnold with $\eta_{grains} = (1/32)^2\sqrt{2D_2^2}$; and (e) the $\mu(I)$ -rheology with no advection term $u_j\partial_j\mu_i$ in the total derivative. Times are $\bar{t} = 0, 1, 2, 3$ and 4.

depending on the ratio of the tangential to the normal stress is not described. The flow never stops (figure 14d). To create a flow threshold, one needs to introduce a divergence of the viscosity, taking into account the jamming transition, or introduce a second contribution standing for the compressive stress (as in Josserand, Lagr e & Lhuillier 2004). Doing so, however, is far from trivial. In the following, we only consider a Bagnold viscosity without introducing a flow threshold. As a consequence, we do not obtain an inner core, which remains essentially static during the collapse, nor do we reproduce the arrest phase of the flow.

4.1.4. Neglecting nonlinear terms

In this part, we investigate the effect of neglecting nonlinear terms. We have carried out a collapse using the $\mu(I)$ continuum but with a linearized total derivative in the Navier–Stokes equation leading to an unsteady Stokes $\mu(I)$. The results are displayed in figure 14(e) for a column of aspect ratio $a = 6.26$, at instants $t\sqrt{g/H_0} = 0, 1, 2, 3, 4$. We observe that the shape of the flow strongly differs from what is observed for a granular material, involving the formation of a wave-like structure. This structure disappears during the propagation, so that the final state is closer to the granular phenomenology than the transient flow is. The fact that the nonlinear advection terms are not negligible for the column collapse highlights the fact that inertia is important relative to viscous dissipation in this particular case.

4.1.5. The constant friction model

The $\mu(I)$ -rheology relates the frictional properties of the flow to the inertial number I , which changes during the flow; as seen in § 3.2, this model reproduces the granular column collapse with a good accuracy. However, one can question the performance of the $\mu(I)$ model compared to a simple constant friction model $\mu = \text{cst} = \mu_s$.

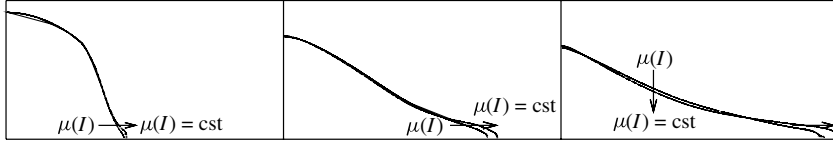


FIGURE 15. A collapse at time $t/(H_0/g)^{1/2} = 1, 2$ and 3 , with aspect ratio $a = 1.42$, with $\mu_s = 0.32$, $I_0 = 0.4$ and $\Delta\mu = 0.28$ in the three panels. In each panel, the same case with a constant $\mu(I) = 0.33$ (cst) is plotted; the arrow is from the variable $\mu(I)$ to the constant $\mu(I) = 0.33$.

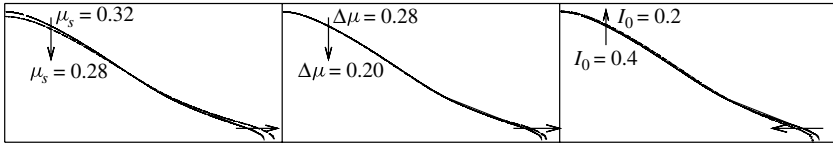


FIGURE 16. A collapse at time $\bar{t} = t/(H_0/g)^{1/2} = 2$ with aspect ratio $a = 1.42$, with $\mu_s = 0.32$, $I_0 = 0.4$ and $\Delta\mu = 0.28$ is shown in the three panels. In each panel, a second computation with only one parameter changed is displayed: (left panel) μ_s is decreased, $\Delta\mu$ and I_0 preserved; (centre panel) smaller $\Delta\mu$, but same $I_0 = 0.4$ and $\mu_s = 0.32$; (right panel) smaller I_0 , but same $\Delta\mu = 0.28$ and $\mu_s = 0.32$.

One example is given in figure 15, where the shape of the collapsing column at three different times for $a = 1.42$ is displayed for the constant friction continuum simulations $\mu(I) = 0.33$ and the case $\mu(I) = 0.32 + 0.28/(0.4/I + 1)$ for comparison. The beginning of the collapse (namely $\bar{t} \lesssim 1.5$) shows a good agreement between the constant friction and $\mu(I)$ models. However, as the flow develops, the agreement between the constant friction model and the granular model degrades; the spreading and flow arrest are best captured by the $\mu(I)$ model. This good agreement at initial times is due to the fact that I is initially small. The same holds for small a , so that good agreement between the $\mu(I)$ and constant friction models is obtained for $a = 0.5$ (not shown). For larger a , the difference increases and a larger μ_s needs to be taken to recover an acceptable solution. However, this rather good performance of the constant friction model questions the actual relevance of the shape of the $\mu(I)$ dependence. This aspect is discussed further in the next section.

4.2. Sensitivity to the shape and parameters of the $\mu(I)$ -rheology

The results discussed so far indicate that the $\mu(I)$ -rheology is able to capture the dynamics of highly transient granular flows. Indeed, the complex evolution of the granular column collapse, for a wide range of aspect ratios, was recovered with very good accuracy. However, the fair (although less good) results obtained with a constant friction model question the sensitivity of the results on the particular shape of the I dependence as well as the value of the rheological parameters. Furthermore, the continuum simulations proved unable to reproduce the last stages of granular flow front propagation. These aspects are discussed next.

What is the sensitivity of the results for the collapsing column to the rheological parameters ($\mu_s, \Delta\mu, I_0$)? As a first quick visual inspection, figure 16 displays three snapshots at the same time, of the same initial column, but on each of the images a second computation is shown where a single parameter is changed. We observe that a decrease of μ_s (every other parameter being fixed) increases the displacement

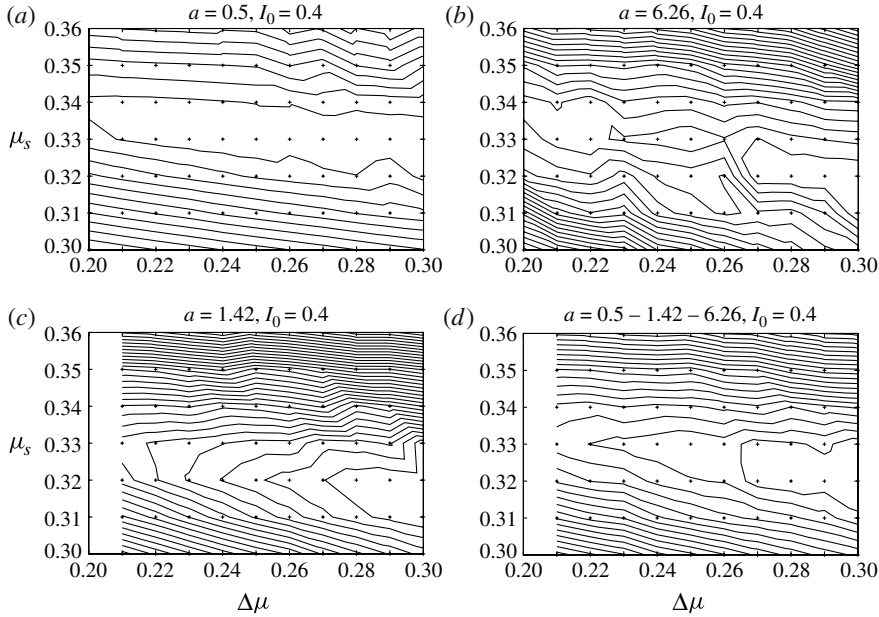


FIGURE 17. Example of isolines (one isoline every 0.03 grain) of the errors between Navier–Stokes and contact dynamic solutions as functions of μ_s and $\Delta\mu$, here for $I_0 = 0.4$: (a) $a = 0.5$ (minimum error 0.65 grain, maximum 2.56 grain); (b) $a = 1.4$ (minimum error 1.36 grain, maximum 3.65 grain); (c) $a = 6.26$ (minimum error 2.06 grain, maximum 4.36 grain); (d) averaged error for the three cases $a = 0.5, 1.4, 6.26$ (minimum error 1.36 grain, maximum 2.39 grain).

of the front and decreases the height. A decrease in $\Delta\mu$ has the same effect, and a decrease in I_0 has the opposite effect. These behaviours are consistent with what is expected from the $\mu(I)$ dependence: a decrease in one of the parameters ($\mu_s, \Delta\mu, 1/I_0$) increases the total friction. To better quantify this sensitivity, we performed a systematic campaign of comparisons. We considered the three cases $a = 0.5, a = 1.42$ and $a = 6.26$. For each case, simulations were performed with μ_s varying in the range $[0.3, 0.36]$, $\Delta\mu$ varying in the range $[0.2, 0.3]$ and I_0 varying in the range $[0.3, 0.4]$. The error for each case was evaluated as the difference between the height profile of the continuum model and the height profile of the granular results integrated over time and over the shape of the deposit. This barycentric mean gives less weight to the front of the flow (which is not so well predicted, as discussed later). An example of the resulting error maps (for $I_0 = 0.4$) is illustrated in figure 17. The optimal parameter set depends on a . For example, the higher a , the higher the value of $(\mu_s, \Delta\mu, 1/I_0)$. To obtain the optimal parameter set over the whole range of aspect ratios, we created a single error map by averaging error maps for individual aspect ratios (bottom right on figure 17) – the error is only 1.36 grain. This resulted in the $(\mu_s = 0.32, \Delta\mu = 0.28, I_0 = 0.4)$ combination used as default in the results presented earlier.

The isolines of error are tilted more or less in a direction corresponding to $\Delta\mu_s/I_0$ constant. This corresponds to a linear contribution $\mu(I) \simeq \mu_s + I\Delta\mu/I_0$ for small enough I . A linear formulation $\mu(I) = \mu_s + bI$ with $\mu_s \sim 0.25$ and $b \sim 1.1$ was initially proposed by da Cruz (2004), da Cruz *et al.* (2005) and GdR MiDi (2004). This shape

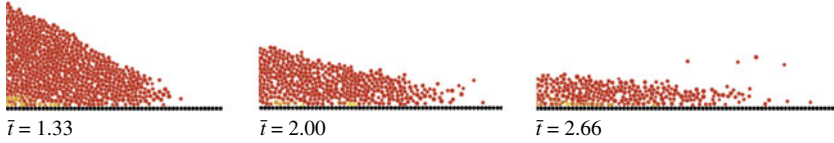


FIGURE 18. (Colour online) Snapshots of the flow front at $\bar{t} = 1.33$, $\bar{t} = 2.00$ and $\bar{t} = 2.66$ for a discrete numerical simulation with aspect ratio $a = 6.26$. Note the rough plane obtained by ‘gluing’ grains.

was then further refined to best-fit the experimental data by Jop *et al.* (2006) in (2.3), namely, $\mu(I) = \mu_s + I\Delta\mu/(I_0 + I)$, which is the formulation followed in the present work. We also tested a linear rheology, which showed good agreement for small I (as expected from figure 17); however, the lack of saturation led to discrepancies for larger I . This tends to confirm the relevance of the $\mu(I)$ -rheology of Jop *et al.* (2006), although other dependences have also been proposed: for example, a power law of I in Hatano (2007); or a square dependence in I , i.e. $\mu(I) = \mu_s + \mu_T I^2$, in Josserand *et al.* (2004).

4.3. Modelling the front of the flow

Although the continuum simulations describe the acceleration stage of the column collapse very well, they are not as accurate during the deceleration phase, when the flow front slows down and eventually stops. The propagation of the flow front is in effect a ‘moving contact line’ problem, a well-known and difficult problem in fluid mechanics even in the case of Newtonian fluids (Pomeau 2002). From the point of view of the contact point, the no-slip condition implemented in Gerris is in effect analogous to a Navier slip condition with a slip length comparable to the mesh size (this is due to the finite-volume representation). This allows for propagation of the contact line but is unlikely to be physically meaningful. Obtaining a consistent description of the flow front is thus likely to require a contact line model itself consistent with the $\mu(I)$ -rheology in the vicinity of the contact line. This was done for early global models of $\mu(I)$ – when I was averaged as a Froude number (Pouliquen 1999). This is a difficult problem whose solution will probably require further advances in the description of contact lines, starting with Newtonian fluids.

Another difficulty lies in the fact that the tip of the flow is formed by a cloud of bouncing grains where binary collisions tend to replace long-lasting frictional contacts. The snapshots of figure 18, showing the granular flow front in the case $a = 6.26$, illustrate this point. Consistently, the values computed by Gerris for the inertial number I in this part of the flow are of the order of one (between one and two, and larger on the final points), which is significantly larger than the typical values for which the $\mu(I)$ relationship was established (GdR MiDi 2004). It thus seems reasonable to suspect that the $\mu(I)$ -rheology, valid in the denser bulk of the flow, may become inaccurate when the volume fraction becomes too low. Alternatively, kinetic theory may provide a framework to capture this part of the flow (Jenkins & Savage 1983). More fundamentally, moving closer to the tip of the flow front, the number of grains involved in the flow rapidly decreases, so that the definition of a representative elementary volume in this area becomes problematic. While statistical properties can be defined in the bulk, this is hardly the case at the very front. In other words, the continuum mechanics assumptions may become invalid at the tip of the flow.

5. Conclusion

While the formulation of constitutive equations for granular flows remains an active field of research, our aim in this contribution was to test the performance of the empirical $\mu(I)$ -rheology using the well-characterized column collapse experiment. To do so, we have developed a continuum simulation tool for dry granular flows by implementing a $\mu(I)$ -dependent viscosity in a complete Navier–Stokes solver (Gerris), using a VOF approach. In contrast to previous works using averaged shallow-layer approximations, we solve the complete velocity field of the equivalent continuum medium. Although the results presented in this paper were two-dimensional, the current implementation in Gerris should also work in three dimensions.

In a series of preliminary numerical tests, we first considered the simple case of a single infinite layer flowing over an inclined plane, for which analytical solutions exist, followed by the case of an infinite granular layer covered with a viscous layer, for which ODEs can be solved. Comparing the solutions of the Gerris solver with the analytical and semi-analytical solutions, we were able to validate the implementation of the $\mu(I)$ -rheology for simple gravity-driven shear flows. Moreover, we were able to show that the existence of a surrounding fluid of lower density and viscosity (air, for instance) did not significantly perturb the behaviour of the granular flow, so that the two-phase approach adopted by Gerris was suitable for the simulation of dry granular systems in air without modifying the shape of the $\mu(I)$ dependence.

Applying the same tool to the granular column collapse experiment, we then considered several column geometries of aspect ratios a varying from 0.25 to 67.9. In addition to continuum simulations, two-dimensional granular simulations using the contact dynamics algorithm were performed to allow for systematic comparison of the shape of the falling column, the position of the front in the course of time and the final run-out. For aspect ratios 0.5, 1.42 and 6.26, the outer and inner deformations of the collapsing column showed good agreement between the two methods. Then by varying the value of the aspect ratio between 0.25 and 64, continuum simulations led to scaling laws linking run-out and final height to aspect ratio in good agreement with experimental scaling laws. The position of the flow front in the course of time shows the same behaviour for both continuum and granular methods during the greater part of the spreading dynamics. Close to arrest, however, continuum simulations systematically underestimate the run-out in the case of large aspect ratios. Finally, considering the extreme case of $a = 67.9$, continuum simulation proved able to reproduce the formation and the outward propagation of a bump as observed in the granular counterpart.

The ability of the $\mu(I)$ -rheology to reproduce the dynamics of the granular collapse was then compared to the performances of some simple model rheologies: Newtonian, Bingham, Bagnold, and the case of constant friction. Of these alternatives, only the constant friction model leads to reasonable results, provided the friction constant is varied according to the aspect ratio. This supports a more complex dependence, and we indeed demonstrate that the additional degrees of freedom of the $\mu(I)$ -rheology can be used to obtain a single ‘optimal’ set of rheological parameters, which describes the collapse accurately across the whole range of aspect ratios (using the contact dynamics simulations as reference).

The value of I becoming noticeably high at the flow front (where volume fraction decreases and bouncing dynamics takes place), the friction coefficient at this point may be overestimated, and may result in the underestimation of the final run-out by the continuum model. It is, however, uncertain whether the $\mu(I)$ -rheology applies at all at

the tip of the front, where grains are in a nearly gaseous state, and where their number is small enough to question the validity of continuum modelling.

Only dry granular flows have been considered so far, but an interesting perspective is to introduce in the present model the physics of immersed dense granular flows (Cassar *et al.* 2005; Chauchat & Médale 2010; Rondon *et al.* 2011). Wider perspectives of this work include the efficient simulation of real systems such as geophysical flows or industrial handling of granular matter: the two-dimensional continuum simulations presented here only take a few minutes to run on a standard PC. Moreover, the work provides a new approach to validate and possibly improve Saint-Venant/shallow-layer approaches.

The complete two-dimensional continuum simulations presented in this paper support the reliability of the $\mu(I)$ -rheology to capture the dynamics of dry gravity-driven non-uniform transient granular flows (beside steady shear), at least in two dimensions. They are reproducible, and now part of the Gerris test suite (Lagrée 2010; Popinet 2011). We next plan to study the flow structure of the continuum model in more detail. We also hope that further applications in more severe configurations (three-dimensional, moving boundaries, etc.) will confirm these encouraging first results.

REFERENCES

- ANCEY, C., COUSSOT, P. & EVESQUE, P. 1999 A theoretical framework for granular suspensions in a steady simple shear flow. *J. Rheol.* **43**, 1673–1699.
- ARANSON, I. S. & TSIMRING, L. S. 2001 Continuum description of avalanches in granular media. *Phys. Rev. E* **64**, 020301.
- BAGNOLD, R. G. 1954 Experiments of gravity-free dispersion of large solid spheres in a Newtonian fluid under shear. *Proc. R. Soc. Lond. A* **255**, 49.
- BAGUÉ, A., FUSTER, D., POPINET, S., SCARDOVELLI, R. & ZALESKI, S. 2010 Instability growth rate of two-phase mixing layers from a linear eigenvalue problem and an initial value problem. *Phys. Fluids* **22**, 092104.
- BALMFORTH, N. J. & KERSEWELL, R. R. 2005 Granular collapse in two dimensions. *J. Fluid Mech.* **538**, 399–428.
- BELL, J. B., COLELLA, P. & GLAZ, H. M. A second-order projection method for the incompressible Navier–Stokes equations. *J. Comput. Phys.* **85**, 257–283.
- BOUCHUT, F., FERNÁNDEZ-NIETO, E. D., MANGENEY, A. & LAGRÉE, P.-Y. 2008 On new erosion models of Savage–Hutter type for avalanches. *Acta Mechanica* **199** (1–4), 181–208.
- CASSAR, C., NICOLAS, M. & POULIQUEN, O. 2005 Submarine granular flows down inclined planes. *Phys. Fluids* **17**, 103301.
- CAWTHORN, C. J. 2011 Several applications of a model for dense granular flows. PhD thesis, University of Cambridge.
- CHAUCHAT, J. & MÉDALE, M. 2010 A three-dimensional numerical model for incompressible two-phase flow of a granular bed submitted to a laminar shearing flow. *Comput. Meth. Appl. Mech. Engrg* **199**, 439–449.
- COURRECH DU PONT, S., GONDRET, P., PERRIN, B. & RABAUD, M. 2003 Wall effects on granular heap stability. *Europhys. Lett.* **61** (4), 492–498.
- CROSTA, G. B., IMPOSIMATO, S. & RODDEMAN, D. 2009 Numerical modelling of 2-D granular step collapse on erodible and nonerodible surface. *J. Geophys. Res.* **114**, F03020.
- DA CRUZ, F. 2004 Écoulements de grains secs: frottement et blocage. Thèse de l'École Nationale des Ponts et Chaussées <http://pastel.paristech.org/archive/946/>.
- DA CRUZ, F., EMAM, S., PROCHNOW, M., ROUX, J.-N. & CHEVOIR, F. 2005 Rheophysics of dense granular materials: discrete simulation of plane shear flows. *Phys. Rev. E* **72**, 021309.
- DAERR, A. & DOUADY, S. 1999 Sensitivity of granular surface flows to preparation. *Europhys. Lett.* **47** (3), 324–330.

- DAVIES, T., MCSAVENEY, M. & KELFOUN, K. 2010 Runout of the Socompa volcanic debris avalanche, Chile: a mechanical explanation for low basal shear resistance. *Bull. Volcanol.* **72** (8), 933–944.
- DOYLE, E. E., HUPPERT, H. E., LUBE, G., MADER, H. M. & SPARKS, R. S. J. 2007 Static and flowing regions in granular collapses down channels: insights from a sedimenting shallow water model. *Phys. Fluids* **19**, 106601.
- DUFOUR, F. & PIJAUDIER-CABOT, G. 2005 Numerical modelling of concrete flow. Homogeneous approach. *Intl J. Numer. Anal. Meth. Geomech.* **29**, 395–416.
- FUSTER, D., AGBAGLAH, G., JOSSERAND, C., POPINET, S. & ZALESKI, S. 2009a Numerical simulation of droplets, bubbles and waves: state of the art. *Fluid Dyn. Res.* **41**, 065001.
- FUSTER, D., BAGUÉ, A., BOECK, T., LE MOYNE, L., LEBOSSETIER, A., POPINET, S., RAY, P., SCARDOVELLI, R. & ZALESKI, S. 2009b Simulation of primary atomization with an octree adaptive mesh refinement and VOF method. *Intl J. Multiphase Flow* **35** (6), 550–565.
- GDR MIDI, 2004 On dense granular flows. *Eur. Phys. J. E* **14**, 341–365.
- HATANO, T. J. 2007 Power-law friction in closely packed granular materials. *Phys. Rev. E* **75**, 060301.
- HOGG, A. J. 2007 Two-dimensional granular slumps down slopes. *Phys. Fluids* **19**, 093301.
- JENKINS, J. T. & SAVAGE, S. B. 1983 A theory for the rapid flow of identical, smooth, nearly elastic, spherical particles. *J. Fluid Mech.* **130**, 187–202.
- JOP, P., FORTERRE, Y. & POULIQUEN, O. 2005 Crucial role of sidewalls in granular surface flows: consequences for the rheology. *J. Fluid Mech.* **541**, 167–192.
- JOP, P., FORTERRE, Y. & POULIQUEN, O. 2006 A rheology for dense granular flows. *Nature* **441**, 727–730.
- JOSSERAND, C., LAGRÉE, P.-Y. & LHUILLIER, D. 2004 Stationary shear flows of dense granular materials: a tentative continuum modelling. *Eur. Phys. J. E* **14**, 127.
- JOSSERAND, C., LAGRÉE, P.-Y. & LHUILLIER, D. 2006 Granular pressure and the thickness of a layer jamming on a rough incline. *Europhys. Lett.* **73** (3), 363–369.
- JOSSERAND, C., LAGRÉE, P.-Y., LHUILLIER, D., POPINET, S., RAY, P. & STARON, L. 2009 The spreading of a granular column from a Bingham point of view. In *Powders and Grains, AIP Conference Proceedings*, vol. 000, pp. 631–634. American Institute of Physics.
- KELFOUN, K., SAMANIEGO, P., PALACIOS, P. & BARBA, D. 2009 Testing the suitability of frictional behaviour for pyroclastic flow simulation by comparison with a well-constrained eruption at Tungurahua volcano (Ecuador). *Bull. Volcanol.* **71** (9), 1057–1075.
- KERSWELL, R. R. 2005 Dam break with Coulomb friction: a model for granular slumping? *Phys. Fluids* **17**, 057101.
- LACAZE, L. & KERSWELL, R. R. 2009 Axisymmetric granular collapse: a transient three-dimensional flow test of viscoplasticity. *Phys. Rev. Lett.* **102**, 108305.
- LACAZE, L., PHILLIPS, J. C. & KERSWELL, R. R. 2008 Planar collapse of a granular column: experiments and discrete element simulations. *Phys. Fluids* **20**, 063302.
- LAGRÉE, P.-Y. 2010 Bagnold flow of a granular material: <http://gerris.dalembert.upmc.fr/gerris/tests/tests/poiseuille.html#toc11>.
- LAJEUNESSE, E., MANGENEY-CASTELNEAU, A. & VILOTTE, J.-P. 2004 Spreading of a granular mass on an horizontal plane. *Phys. Fluids* **16**, 2371–2381.
- LAJEUNESSE, E., MONNIER, J. B. & HOMSY, G. M. 2005 Granular slumping on a horizontal surface. *Phys. Fluids* **17**, 103302.
- LAJEUNESSE, E., QUANTIN, C., ALLEMAND, P. & DELACOURT, C. 2006 New insights on the runout of large landslides in the Valles–Marineris canyons. *Mars Geophys. Res. Lett.* **33**, L04403.
- LARRIEU, E., STARON, L. & HINCH, E. J. 2006 Raining into shallow water as a description of the collapse of a column of grains. *J. Fluid Mech.* **554**, 259–270.
- LUBE, G., HUPPERT, H. E., SPARKS, R. S. J. & HALLWORTH, M. A. 2004 Axisymmetric collapses of granular columns. *J. Fluid Mech.* **508**, 175–199.
- LUBE, G., HUPPERT, H. E., SPARKS, R. S. J. & FREUNDT, A. 2005 Collapses of two-dimensional granular columns. *Phys. Rev. E* **72**, 041301.

- MANGENEY, A., ROCHE, O., HUNGR, O., MANGOLD, X. X. X., FACCANONI, G. & LUCAS, A. 2010 Erosion and mobility in granular collapse over sloping beds. *J. Geophys. Res.* **115**, F03040.
- MANGENEY-CASTELNAU, A., BOUCHUT, F., VILOTTE, J. P., LAJEUNESSE, E., AUBERTIN, A. & PIRULLI, M. 2005 On the use of Saint Venant equations to simulate the spreading of a granular mass. *J. Geophys. Res.* **110**, B09103.
- MILLS, P., LOGGIA, D. & TIXIER, M. 1999 Model for a stationary dense granular flow along an inclined wall. *Europhys. Lett.* **45** (6), 733–738.
- MOREAU, J.-J. 1994 Some numerical methods in multibody dynamics: application to granular materials. *Eur. J. Mech. A* **4**, 93–114.
- NICHOL, K., ZANIN, A., BASTIEN, R., WANDERSMAN, E. & VAN HECKE, M. 2010 Flow-induced agitations create a granular fluid. *Phys. Rev. Lett.* **104**, 078302.
- PAILHA, M. & POULIQUEN, O. 2009 A two-phase flow description of the initiation of underwater granular avalanches. *J. Fluid Mech.* **633**, 115–135.
- POMEAU, Y. 2002 Recent progress in the moving contact line problem: a review. *C. R. Acad. Sci. Paris* **330**, 207–222.
- POPINET, S. 2003 Gerris: a tree-based adaptive solver for the incompressible Euler equations in complex geometries. *J. Comput. Phys.* **190** (2), 572–600.
- POPINET, S. 2005 Creeping Couette flow of generalised Newtonian fluids: <http://gerris.dalembert.upmc.fr/gerris/tests/tests/couette.html>.
- POPINET, S. 2009 An accurate adaptive solver for surface-tension-driven interfacial flows. *J. Comput. Phys.* **228**, 5838–5866.
- POPINET, S. 2011 Collapse of a column of grains: <http://gerris.dalembert.upmc.fr/gerris/wiki/index.php/Examples>.
- POULIQUEN, O. 1999 On the shape of granular fronts down rough inclined planes. *Phys. Fluids* **11** (7), 1956–1958.
- POULIQUEN, O. & FORTERRE, Y. 2009 A non-local rheology for dense granular flows. *Phil. Trans. R. Soc. A* **367**, 5091–5107.
- POULIQUEN, O. & FORTERRE, Y. 2002 Friction law for dense granular flows: application to the motion of a mass down a rough inclined plane. *J. Fluid Mech.* **453**, 133–151.
- RONDON, L., POULIQUEN, O. & AUSSILLOUS, P. 2011 Granular collapse in a fluid: role of the initial volume fraction. *Phys. Fluids* **23**, 073301.
- SAVAGE, S. B. 1979 Gravity flow of cohesionless granular materials in chutes and channels. *J. Fluid Mech.* **92**, 53–96.
- SAVAGE, S. & HUTTER, K. 1989 The motion of a finite mass of granular material down a rough incline. *J. Fluid Mech.* **199**, 177–215.
- SCHLICHTING, H. 1987 *Boundary Layer Theory*, 7th edn. McGraw-Hill.
- STARON, L. & HINCH, E. J. 2005 Study of the collapse of granular columns using two-dimensional discrete-grain simulation. *J. Fluid Mech.* **545**, 1–27.
- STARON, L. & HINCH, E. J. 2007 The spreading of a granular mass: role of grain properties and initial conditions. *Granular Matter* **9**, 205–217.
- STARON, L., LAGRÉE, P.-Y., JOSSEAND, C. & LHUILLIER, D. 2010 Flow and jamming of two-dimensional granular bed: towards a non-local rheology? *Phys. Fluids* **22**, 113303.
- VOLA, D., BABIK, F. & LATCHÉ, J.-C. 2004 On a numerical strategy to compute gravity currents of non-Newtonian fluids. *J. Comput. Phys.* **201** (2), 397–420.
- ZENIT, R. 2005 Computer simulations of the collapse of a granular column. *Phys. Fluids* **17**, 031703.